Illuminating the Principles of Partial Glucose Oxidation in Aqueous Solution with Molecular Oxygen Using Gold Catalysts on Carbonaceous Model Supports

Master Thesis

Dipl.-Chem. Milena Perović

In the group of Dr. Martin Oschatz

First Examiner: Prof. Dr. Christina Roth

Second Examiner: Prof. Dr. Dr. h.c. Markus Antonietti

Berlin, 15.02.2018

Erklärung

Ich versichere, dass ich die vorgelegte Masterarbeit am Max-Planck-Institut für Kolloid- und Grenzflächenforschung in Potsdam in der Zeit vom 01.08.2017 bis 01.02.2018 in der Forschungsgruppe von Herrn Prof. Dr. Dr. h.c. Markus Antonietti unter der Anregung und Anleitung von Herrn Dr. Martin Oschatz selbstständig durchgeführt und keine anderen als die angegebenen Hilfsmittel und Quellen benützt habe.

Berlin, den 15.02.2018   …………………………

                                                    Milena Perović

Acknowledgments

I would like to thank Prof. Markus Antonietti for giving me this extremely valuable opportunity to complete my master thesis within his group. I would like to acknowledge Prof. Christina Roth of the Free University Berlin as the internal supervisor of this thesis.

I would like to express my special thanks of gratitude to Dr. Martin Oschatz for supervising my work. I have greatly expanded my knowledge and gained a lot of valuable skills during my master thesis, which would be impossible without Martin's excellent mentoring.

I would like to thank CC Carbon (AG Oschatz) for sharing their experiences, giving me advices and ideas, and encouraging me throughout my time at MPI.

I wish to thank various people for their contribution to this project: Ms Heike Runge, for TEM images; Ms Jeannette Steffen for ICP measurements; Ms Ingrid Zenke for SAXS measurements; Ms Ankita Malik for HPLC measurements and Mr Ralf Walczak for water vapor adsorption isotherms.

I would like to thank DAAD for financially supporting my studies through scholarship for graduate students.

I would like to offer my special thanks to my friends and family for a great support throughout my studies. It would be impossible to complete my studies without them by my side.

Contents

Abstract

Nanocarbon materials are attractive catalyst supports, due to their chemical and thermal stability, as well as their weak chemical interaction with the metal particles, which are employed as active species in catalytic reactions. Support effects on catalytic activity of heterogeneous gold nanoparticle catalysts for the selective oxidation of D-glucose to D-gluconic acid in aqueous solution with molecular oxygen are investigated. The advantage of carbon materials over traditional oxide supports is reported. Moreover, the influence of different gold loadings with carbonaceous supports of various porosities is studied. High Au loadings are proven to be the least efficient for the series of carbon-supported catalysts, whereas theoretical gold loading of 1 wt. % or below on carbon generally exhibits the highest metal-based catalytic activities. Significant activity at higher metal loading can only be achieved with selected supports of tailored mesoporosity. Series of catalysts that provide high metal time yield (up to 3 $mol_{glucose}/mol_{Au}/s$) for glucose oxidation reaction have been successfully synthesized. The most versatile catalyst support, offering broad range of possible Au loadings while preserving high catalytic activity is newly synthesized ordered mesoporous hard-salt templated carbon (OMHSTC) resulting from its well suited mesoporosity.

1. Introduction

1.1 Heterogeneous Catalysis

Catalysis makes use of small amounts of foreign substances (*catalysts*) for acceleration of chemical reactions. Catalysis is a cyclic process, in which a catalyst converts reactants into products, through a series of elementary steps, while being regenerated to its original form at the end of each cycle during its lifetime. In most cases, catalysts activate the substrates by breaking or weakening particular chemical bonds and thus change the kinetics of the reaction, but not the position of the thermodynamic equilibrium (**Figure 1**). The catalyzed reaction pathway has lower activation energy (E_a), but the overall energy of reactants and products (reaction enthalpy ΔE) is not affected by the presence of a catalyst.
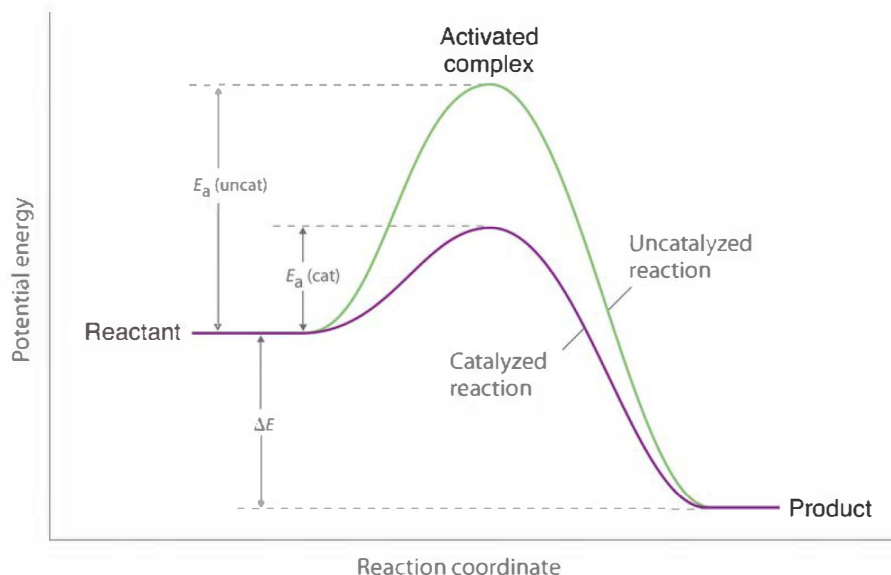
Figure 1. *Potential energy diagram for a single-step exothermic reaction in the presence and absence of a catalyst.* [1]

If the catalyst and reactants are present in the same phase, then the reaction is called homogeneously catalyzed. Typical homogeneous catalysts are organometallic complexes, metal salts of organic acids, carbonyls of Co, Fe, Rh etc. which are typically present in a solution together with the educts and products of the particular reaction. On the other hand, in heterogeneous catalysis, reactants and catalyst form separate physical phases, for example inorganic solids such as metals, oxides, sulfides and metal salts, as well as organic materials such as organic hydroperoxides, ion exchangers and enzymes are solid catalysts which can catalyze

2

reactions between partners in liquid phase (most often in solution) or in gas phase. [2] Some particular types of heterogeneous catalysis include electrocatalysis involving oxidation or reduction by transfer of electrons through an external circuit; photocatalysis, where the catalyst uses light absorption for activation of the reactants; or biocatalysis, in which enzymes or microogranisms are accelerating reactions.

A common way of combining the advantages of homogeneous and heterogeneous catalysis is to immobilize the former using an appropriate solid material (also called the "support") and thus make them "quasi-heterogeneous". The reason for this is to take advantage of usually high selectivity and activity of homogeneous catalysts, while using a key asset of heterogeneous catalysts which is the relative ease of separation from reaction medium and their high stability under harsh conditions. Most widely used inorganic supports include oxidic support materials (TiO_2, SiO_2, γ-Al_2O_3, MgO), carbon materials, zeolites, silicon carbide and many more. In consequence, typical heterogeneous catalysts consist of nanostructured active sites (in most cases metal clusters or metal nanoparticles) which are distributed over the high surface area of such nanoporous supports which can reach up to 2000 m^2/g. [3] [4] [2] The major role of the support is to disperse the metallic active centers and stabilize them under the conditions and for the time of the reaction.

Catalysis must always be preceded by adsorption. The Sabatier principle proposes the existence of an unstable intermediate compound formed between the catalyst surface and at least one of the reactants – stable enough to be formed in sufficient quantities and labile enough to be transferred to the desired product which has to be released from the catalyst surface again. [5]

During a heterogeneous catalytic reaction, there are series of intermediate steps (**Figure 2**) through which generally reactants, catalyst and product(s) are going, briefly summarized as:

1. Diffusion of the reactants through a boundary layer surrounding the catalyst particle.
2. Intra-particle diffusion of the reactants into the catalyst pores to the active sites.
3. Adsorption of the reactants onto active sites.
4. Surface reactions involving formation or conversion of various adsorbed intermediates, possibly including surface diffusion steps.
5. Desorption of products from catalyst sites.
6. Intra-particle diffusion of the products through the catalyst pores.
7. Diffusion of the products across the boundary layer surrounding the catalyst particle. [2]

The step with the highest activation energy determines the rate of the reaction.
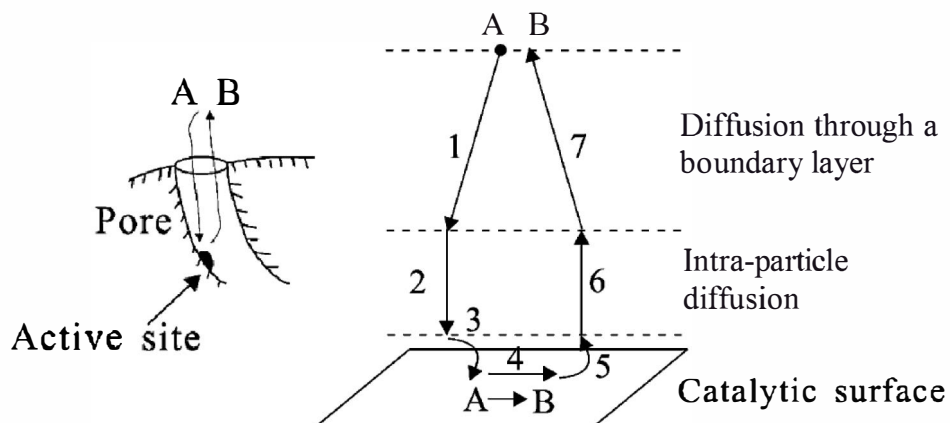
Figure 2. *Intermediate steps in heterogeneous catalysis reaction A → B.* [6]

Three main mechanisms (**Figure 3**) are known to occur during the surface-catalyzed transformations of reactants to yield the products:

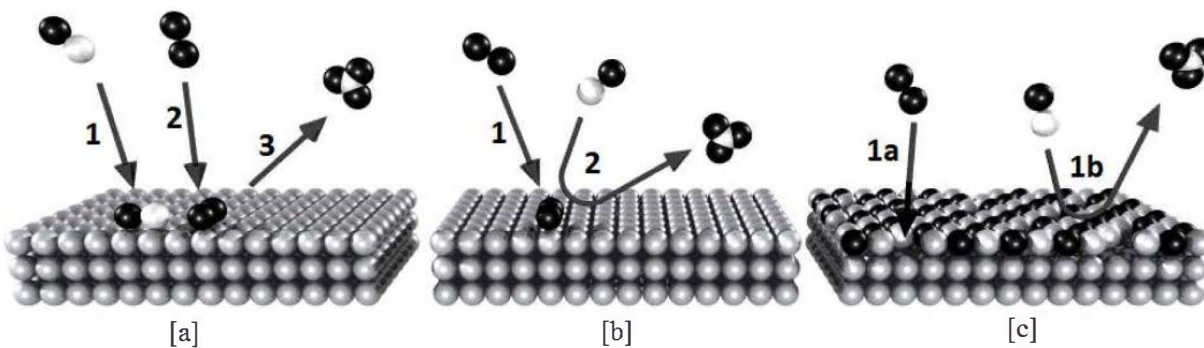**Figure 3.** *Langmuir – Hinshelwood mechanism [a], Eley – Rideal mechanism [b] and Mars – van Krevelen mechanism [c].* [7]

In the case of the Langmuir – Hinshelwood mechanism (**Figure 3a**), both reactant species are attached to the surface, and atomic reorganization takes place in the adsorbed layer. On the contrary, the Eley – Rideal mechanism (**Figure 3b**) describes a process where only one of the reactant species is bound to the catalyst surface, and is converted into product when it comes into a contact with second reactant from the surrounding phase. Finally, in the Mars – van Krevelen mechanism (**Figure 3c**), the surface itself (usually metal oxides, carbides, and sulfides) is an active part in the reaction. One reactant forms a chemical bond with the catalyst surface (reaction 1a), after which other reactant reacts with the atoms from the chemically bonded reactant on the surface (reaction 1b). When the reaction product desorbs, a vacancy is left behind in the surface. [3, 8]

4

Active sites most often include more than one species (or atoms) to form multiplets or ensembles. A mandatory requirement for these sites to be active is that they are accessible for chemisorption from the fluid phase. Therefore, they must provide free coordination sites, which is analogous to homogeneous organometallic catalysts.[2]

The rate of any gas – solid or liquid – solid-catalyzed reaction can be expressed as the product of the apparent rate coefficient k and a pressure- (or concentration-) dependent term:

$$rate = kf(p_i) \tag{1}$$

where p_i is the partial pressure of the reactant i (in the case of liquid reactants, p_i is replaced by concentration of the reactant). Since the rate coefficient changes with changing the reaction conditions (temperature, pressure, surface concentrations, etc.), it is convenient to use the Arrhenius equation:

$$k = A'exp\,(-E'/RT) \tag{2}$$

where A' is a temperature-independent pre-exponential factor and E' is the apparent activation energy of the catalytic reaction. Considering that activation energy cannot be expressed as such in the above equation (because the concentration of reactant at the catalyst surface is temperature-dependent), the catalytic activity should not be expressed in terms of activation energy. Instead, the concept of *turnover frequency* (TOF; *turnover number*, TON; *turnover rate*, TOR) is used. This term defines catalytic activity as number of revolutions of the catalytic cycle n per unit time t, for a fixed set of reaction conditions.

$$TOF = \frac{formed\ number\ of\ molecules\ of\ a\ given\ product}{(number\ of\ active\ sites)\ \text{x}\ (time)}$$

or:

$$TOF = \frac{1}{S}\frac{dn}{dt}$$

$$\tag{3}$$

However, it is often difficult to determine the number of active sites, especially in the case of highly dispersed supported metal nanoparticle catalysts. Therefore, a metal time yield (MTY) is commonly used for defining catalytic activity in such systems, as expressed:

$$MTY = mol\ (reactant)/mol\ (metal)/time \qquad (4)$$

where *mol (reactant)* corresponds to number of moles of reactant converted into products, and *mol (metal)* stands for number of moles of metal which acts as catalyst in the reaction. [9] [3]

Another important feature of a catalyst, together with high activity and long-term stability, is its selectivity, *S*, which reflects its ability to convert the reactants to a specific product, or in other words the ratio of a desired product into the mixture of all products. It is expressed (Equation 5) as a rate of conversion of reactants to a particular product *A* over rate of conversion of reactants to all products *P*.

$$S(A) = \frac{R(A)}{R(P)} \qquad (5)$$

1.2 Gold Nanoparticles in Heterogeneous Catalysis

Nanoparticles are defined as discrete particles between 1 and 100 nm in size. They can be solid or dispersed in water (hydrosols) as well as in organic solvents (organosols). Nowadays, nanoparticles cover a wide range of applications. The most important fields where gold nanoparticles (AuNPs) are used include electronics, therapeutic agent delivery, medical diagnostics and sensors. In electronics, they can be used as conductors from printable inks to electronic chips.[10] Therapeutic agents can be coated onto the surface of gold nanoparticles, due to their large surface area-to-volume ratio.[11] AuNPs are used to detect biomarkers in the diagnosis of hearth diseases, cancers and infectious agents.[12] Wide variety of sensors use gold nanoparticles, some of which include colorimetric sensors, sensors used in surface enhanced Raman spectroscopy and others. [13]

One of their major fields of application is heterogeneous catalysis. Nanoparticles are in most cases the catalytically active sites and the conversion of educts takes place on their surface. As

described above, activation of educt molecules usually takes place on the external surface of the metal particles due to the presence of free binding sites (or electron vacancies) of the surface exposed atoms. Due to their very low diameter, nanoparticles provide a high ratio of surface atoms and thus a large contact area between the active material of the catalyst and the surrounding gas or liquid phase. The fraction of atoms at the surface of a particle is called dispersion, and it scales with surface area divided by volume, that is with the inverse radius or diameter. Dispersion as a function of *n* atoms along an edge and a total of $N = n^3$ atoms is presented in **Figure 4**. Atoms at the surface have less nearest neighbors than atoms in the bulk, which means that particles with a large fraction of atoms at the surface have a low mean coordination number (number of nearest neighbors). [14][15]
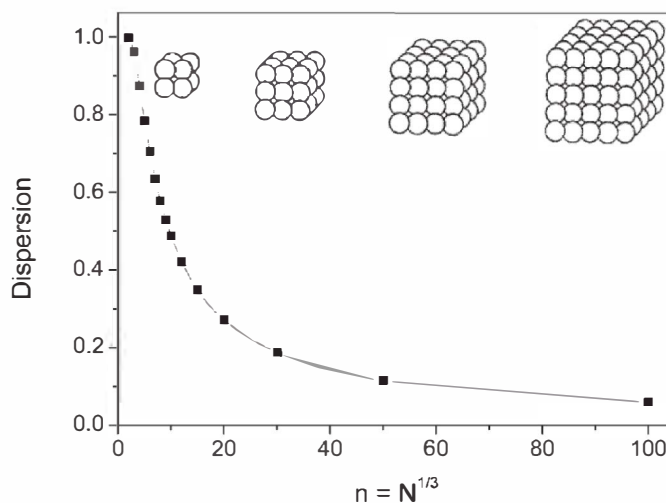

Figure 4. *Dispersion as a function of n for cubic clusters.* [14]

Metal nanoparticles can be obtained by "top-down" and "bottom-up" methods. "Top-down" approaches make use of mechanical grinding of bulk metal and possible subsequent stabilization of the smaller fragments by colloidal protecting agents. On the other hand, "bottom-up" methods of wet chemical nanoparticle preparation typically consist of chemical reduction of metal salts, electrochemical pathways or the controlled decomposition of metastable organometallic compounds.[16][17] The latter method typically enables a more precise control over particle size distribution and allows the formation of smaller particles with a more facile further processing.

Within this work, a "bottom-up" method by chemical reduction of hydrogen tetrachloroaurate(III) trihydrate in the presence of sodium citrate as a stabilizing agent was applied to obtain colloidal gold nanoparticles.[18] The formation of nanoclusters stabilized by

sodium citrate is relying on electrostatic and steric stabilization, creating hydrosols and preventing the aggregation of particles. Moreover, this protecting group is used to control particle size and shape as well as surface properties during synthesis. The importance of this control lies in the fact that aggregation and dispersion properties of nano-sized colloidal particles increases their size and thus govern their optical, electronic and, most importantly for this work, catalytic applications.

Unlike bulk gold, which is chemically rather inert due to its high standard electrode potential (that is, its "nobility"), gold nanoparticles (AuNPs) with size below 10 nm display exceptional catalytic activity, especially in oxidation reactions.[19] In 1998 Prati and Rossi reported that carbon supported gold nanoparticles are capable of catalyzing the oxidation of diols in aqueous phase using oxygen as the stoichiometric oxidant.[20] This is the first report of gold catalyzed alcohol oxidation, and in this report gold is superior to conventional palladium and platinum catalysts. Selective oxidation of cycloalkanes using gold supported on mesoporous silica displayed selectivities higher than 90%. [21] [22] More recent work by Hutchings demonstrated that Au/C is also capable of oxidizing a basic aqueous glycerol solution to form sodium glycerate with 100% selectivity at 56% conversion. [23] Many of these examples indicate that the catalytic properties of gold and gold-containing alloys are notably influenced by the particle size as mentioned above. For instance, Haruta *et al.* showed that the MTY value for the glucose oxidation reaction sharply increases as the diameter of AuNPs decreased from 10 nm (**Figure 5a**), whereas TOFs of CO oxidation over Au/TiO$_2$ exhibit an increase for the particles smaller than 4 nm (**Figure 5b**).[24] [25]
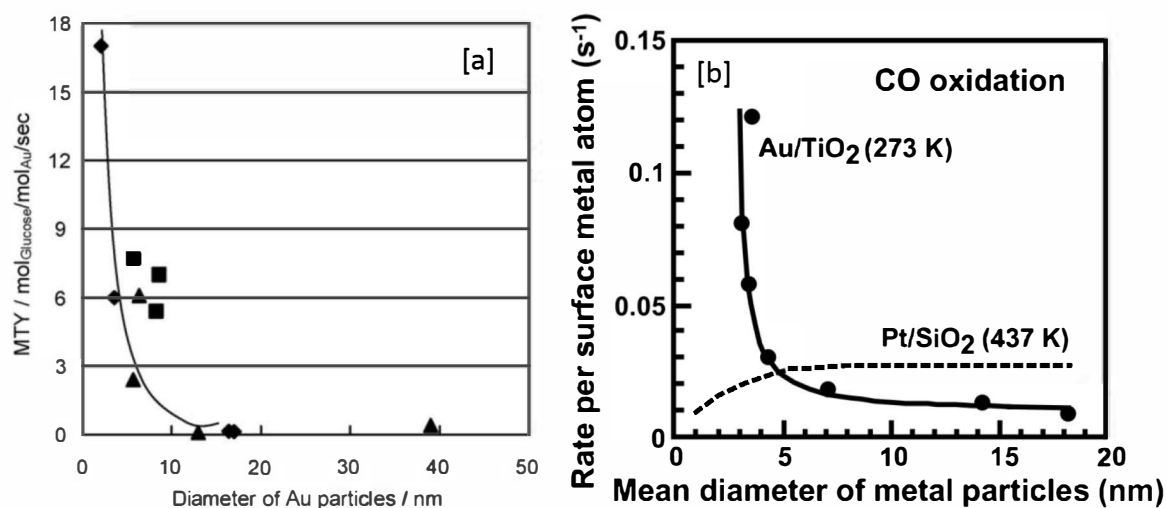

Figure 5. *MTY as a function of AuNP diameter for glucose oxidation reaction [a],[24] and TOF as a function of AuNP diameter for CO oxidation [b].[25]*

Small particles have a relatively large number of low-coordinated Au atoms, which are located at the edges and, in particular, at the corners of particles. [26] [27] [28] [29] [30] [31] [32] These active sites are of course only available if they are not blocked with too strongly adsorbed species, also called "catalyst poisons". In case of gold, especially sulfur species are well known to adsorb irreversibly on the metallic surface which can lead to a loss of catalytic activity.[30] Another requirement to fully utilize the high potential of gold nanoparticles for various oxidation reactions is that excessive particle growth during catalytic operation must be minimized in order to keep the high catalytic activity over a long time. For that purpose, gold nanoparticles are in most cases dispersed over solid supports to minimize their tendency for agglomeration. Especially porous carbon materials are a versatile set of supports for the immobilization of gold nanoparticles, due to their tailorable pore structure and chemical stability. Unlike some other (mainly oxidic) inorganic materials, carbon materials only slightly affect the catalytic properties of AuNPs due to the weak (mainly physical) interaction between metal and carbon surface. [24] [33] [34] [24]

1.3 Porous Carbon Materials as Catalyst Supports

For any metal catalyst it is customary to disperse the nanoparticles homogenously throughout the entire internal surface area of the porous support, in order to create a large specific metal surface area which is entirely accessible in an open pore structure. Furthermore, inter-particular distances have to be maximized with regard to avoid particle agglomeration.

In recent years, there has been large expansion in the number of porous solids, often with significantly different textural and chemical properties. Some of the notable materials encompassed in this group are various kinds of carbons, zeolites, metal oxides, metal- and covalent-organic frameworks (MOFs and COFs) etc. [3] [34] [35] Most of them are widely applied in catalytic processes and benefit from their high specific surface area which, in turn, results from the porous structure.

A surface curvature is defined as a pore if its cavity is deeper than wide. According to the International Union of Pure and Applied Chemistry (IUPAC) recommendation, porous materials can be classified into three types based on their pore diameters: microporous (< 2 nm in diameter), mesoporous (2 – 50 nm) and macroporous (> 50 nm). [36] In addition, pores in solid

materials can be divided into intra-particle pores and inter-particle pores. For instance, carbon nanomaterials with large external surface area such as carbon nanotubes, fullerenes, carbon aerogels, or onion-like carbon are materials with inter-particle pores (**Figure 6**).
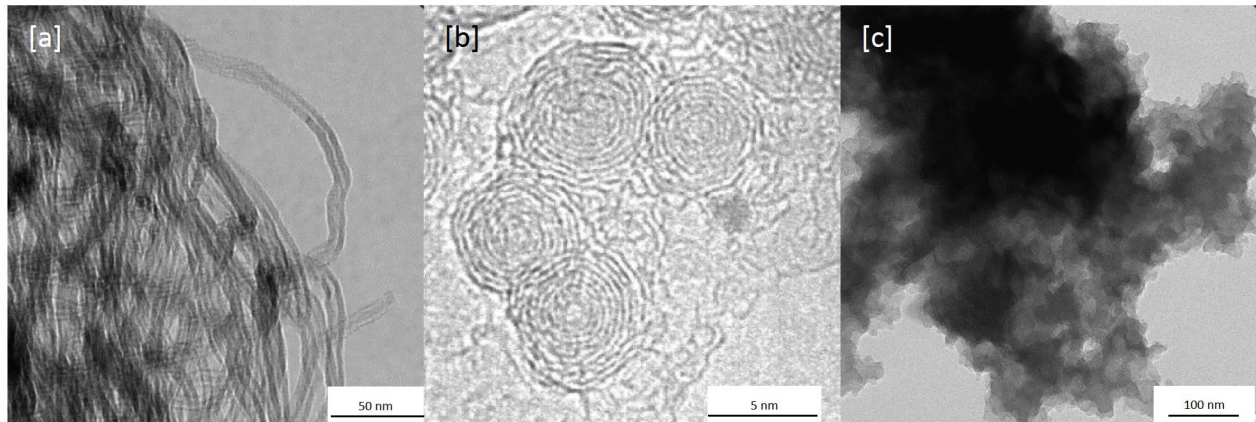

Figure 6. *TEM images of multiwalled carbon nanotubes [a], onion-like carbon [b] and carbon aerogel [c].* [37] [38]

On the other hand, typical porous carbons are characterized by an amorphous carbon microstructure and a high ratio between internal and external porosity and thus surface area (**Figure 7**). [39] [40-42]
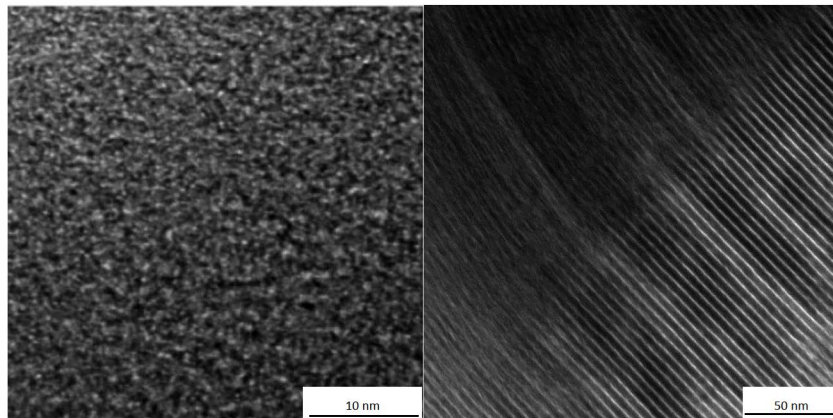

Figure 7. *TEM images of microporous [a]* [43] *and mesoporous carbon [b].*

Porous carbon materials can provide large specific surface areas (SSAs) and total pore volumes (V_t), but what makes them outstanding for application in various fields – such as catalysis, electrochemical energy storage, gas adsorption, biomedicine – is the ability to design their pore size on different levels. When it comes to catalytic utilization, the main advantages that carbon supports offer over most of the traditional oxidic catalyst supports such as silica, alumina, titania, ceria, or zeolites are their resistance to both acidic and basic media, stability at high temperatures,

as well as a weak interaction with deposited metals, i.e. the active species are not oxidized which is in most cases leading to a decrease in activity. Moreover, chemical properties of their surface can be modified to control acidity/basicity, polarity, and hydrophobicity. Porous carbons can be prepared with a variety of macroscopic shapes (e.g., powder, granules, fibers, pellets). Another advantage of carbon supports is that the active phase (metal) can be easily accomplished after the use of the catalyst by simply burning off the carbon support.[44 45 35 33 34]

Two major classes of carbon materials with industrial importance are carbon blacks and activated carbons. Carbon blacks are formed by the incomplete combustion or cracking of hydrocarbon gases and vapors derived from petroleum sources. Two carbon black manufacturing processes (furnace black and thermal black) produce nearly all of the world's carbon blacks, with the furnace black process being the most common. Furnace black process uses heavy aromatic oils as feedstock, whereas thermal black employs natural gas, consisting primarily of methane or heavy aromatic oils. Porosity of resulting carbon material is quite low, with predominantly external pores.[46, 47 34] Activated carbons, on the other hand, use carbon precursors, such as coal, wood, pitch, fruit stones and coconut shells as the most important feedstocks. These sources are carbonized at temperatures above 500°C under inert conditions, yielding microporous carbons. However, specific surface areas of these materials are too low for commercial applications after this process. Therefore, a postmodification of this material in order to increase the porosity is needed. This is referred to as activation, which can be physical (thermal) or chemical. Physical activation makes use of carbon dioxide and water vapor, either individually or together. During these endothermic reactions (Eq. 6 and 7), carbon atoms are "extracted" (or in other words "etched") from the structure of carbon material.

$$C + O_2 \rightarrow 2CO \tag{6}$$

$$C + H_2O \rightarrow CO + H_2 \tag{7}$$

In the case of chemical activation, modifications are made by using phosphoric acid (H_3PO_4), zinc chloride ($ZnCl_2$), or potassium hydroxide (KOH). The use of these inorganic dehydration agents usually leads to higher carbon yield and it is often possible to obtain slightly better defined porosity in comparison with physical activation methods. [47 48] However, neither chemical nor physical activation procedures form very narrowly distributed pores.[49] In the synthesis of carbon materials a precise control over their pore structure is crucial in order to tailor it for the use as catalyst support. Carbon materials with well-defined ("ordered") mesopores can for example be prepared by the so-called nanocasting procedure. Carbon precursors (e.g. sucrose) are infiltrated

into the pore system of ordered mesoporous silica templates followed by carbonization and template removal (**Figure 8**). The pore structure can be precisely controlled by the infiltration and carbonization conditions or by the structure of the silica template. The resulting carbon materials are widely known as CMKs (Carbons Mesostructured by KAIST) and exhibit narrow mesopore size distributions, as well as high SSAs. [50] [51] [52] [42]
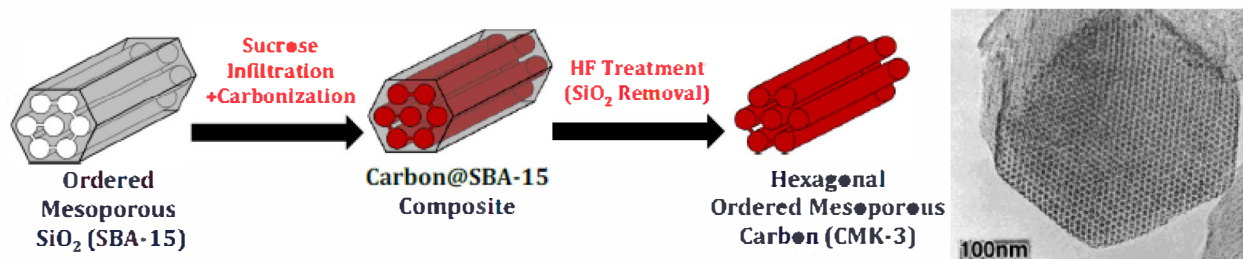

Figure 8. *Synthesis of CMK-3 and TEM image showing the hexagonal ordered pore structure.*[50] [42]

Ordered mesoporous carbon with additional high micropore content and thus a so-called hierarchical pore system can for example be prepared by combination of silica hard templates and salt templates for meso- and micropore formation, respectively as recently reported by Yan *et al*. (**Figure 9**). [53] Salt templating avoids harsh conditions which are applied in other classical strategies for obtaining micropores. The pore size can be regulated by using different salt mixtures (including $LiCl/ZnCl_2$, $NaCl/ZnCl_2$, or $KCl/ZnCl_2$) and by adjusting the component ratios such as the amount of salt in relation to the carbon precursor. [54] [53] Salt and hard templates are removed by evaporating salts during carbonization and washing with NaOH solution, respectively. Sucrose can be utilized as a renewable carbon precursor with excellent accessibility. Resulting ordered mesoporous hard salt templated carbons (OMHSTCs) offer high SSAs and V_ts which are significantly higher than for purely mesoporous CMK-3 obtained from the same silica template. In addition, the ratio of micropores to ordered mesopores, as well as their sizes can be regulated by adjusting the amount of the salt template and the type of hard template.
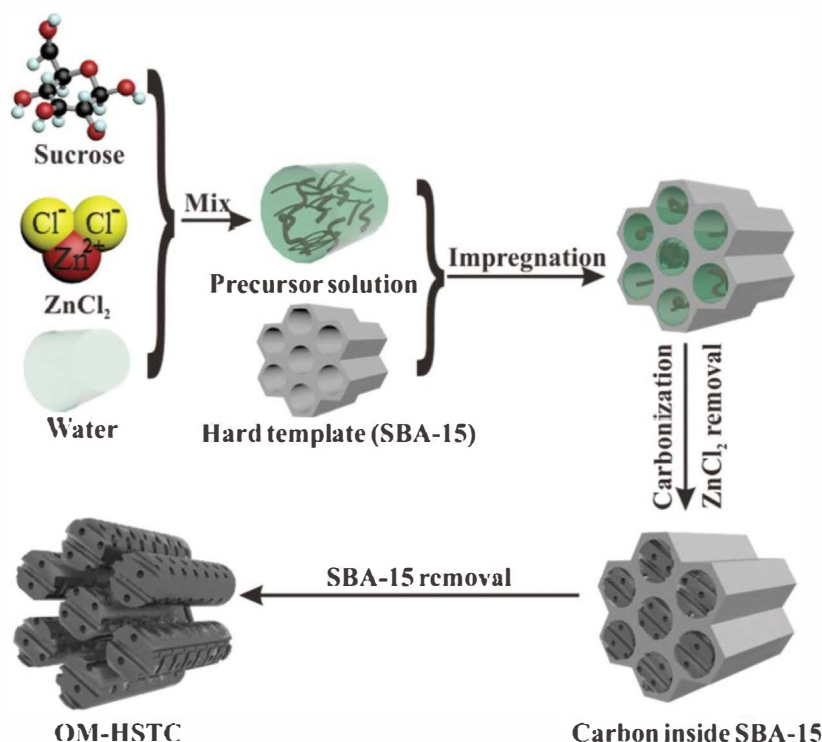
Figure 9. *Preparation of ordered mesoporous hard salt templated carbon (OMHSTC).* [53]

1.4 Glucose Oxidation Reaction

Selective oxidation of the aldehyde group in β-D-glucose to a carboxyl group results in the formation of D-gluconic acid. D-gluconic acid ($C_6H_{12}O_7$) is a colorless to light yellow syrup, non-volatile, harmless, and easily biodegradable aldonic acid, which is soluble in water and insoluble in non-polar solvents. It can be obtained using chemical, electrochemical, catalytic methods and through biotransformation by microorganisms (fungi or bacteria) or their enzymes. D-Gluconic acid is a compound of great importance in the field of food, pharmaceutical, building and textile industry, with its most important application as an additive to dairy products and soft drinks. The production of gluconic acid is estimated to amount of approximately 100,000 t/year and is mainly achieved by oxidation of glucose based on biotechnological fermentation methods. However, there are several drawbacks in these means of obtaining gluconic acid. For instance, the usage of filamentous fungi requires that the process is performed in batches, i.e. continuous operation is impossible. In addition, some type of aerobic bacteria used for gluconic acid production can lead to the formation of side products.[55] However, the developments in the last

two decades have indicated that the heterogeneous catalytic route utilizing supported metal nanoparticles may be a possible alternative on an industrial scale at high space time yield (**Figure 10**). [56] [57] [33]
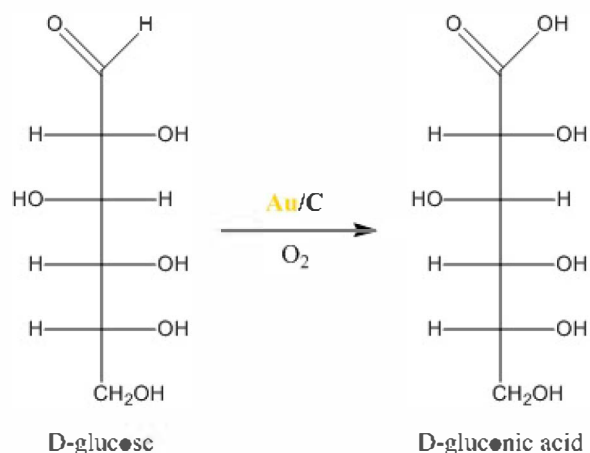

Figure 10. *D-glucose oxidation.*

Various studies employing platinum metal-group catalysts with heavy metals such as bismuth or lead have been reported. The drawbacks of these systems are mainly connected to the catalyst leaching, self-poisoning and over-oxidation, which lead to a conclusion that gold is a superior metal in terms of selectivity and activity. [56] [58] [59] Rossi *et al.* showed that gold allowed much better catalytic activity as compared to Pt group catalysts, reaching TOF value around 3000 mol of reacted glucose (mol total Au h^{-1}) at 50°C (**Figure 11a**). [56]
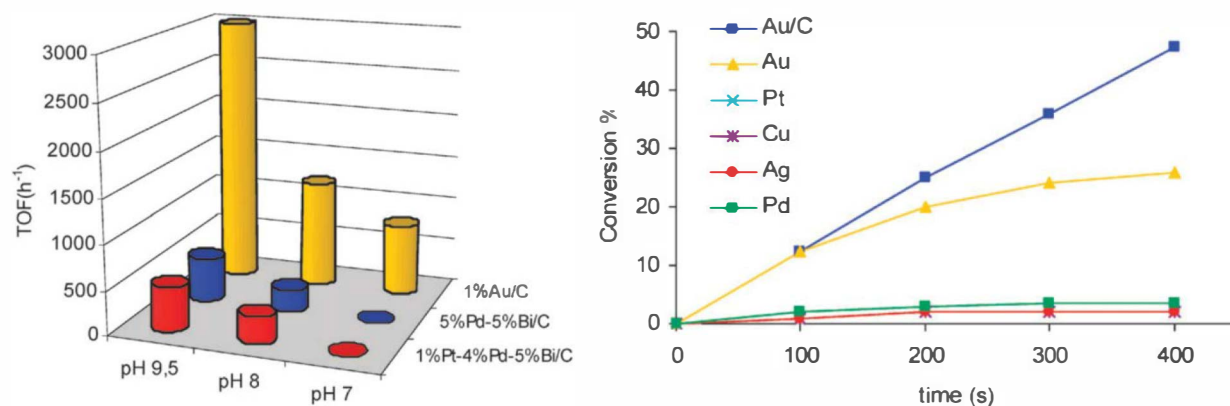

Figure 11. *Catalytic performance of different catalysts for glucose oxidation reaction [a][56], and conversion of glucose as a function of time for different metals [b].* [59]

On the other hand, the influence of different supporting materials on catalytic activity has been investigated, including titania, alumina, silica. [60] [61] [62] Unsupported gold-colloids have been investigated as well, showing lower stability than supported AuNPs, but much better activity than other colloidal metals (**Figure 11b**). [59] There has been an extensive studies using different types of carbon as supports, involving various types of commercially available carbons. [30 63 64 56 65 66 59] Kinetic studies on the selective glucose oxidation carried out using carbon supported AuNPs, proposed that the reaction pathway is following the Langmuir – Hinshelwood model. The oxidative dehydrogenation mechanism, commonly observed in the liquid-phase oxidation of alcohols and aldehydes, is adopted for this reaction. The whole reaction mechanism can be reduced to three elementary reactions, namely, adsorption of glucose, surface reaction of glucose, and desorption of gluconic acid. The rate determining step in this process is the oxidation of glucose by dioxygen dissolved in water. [33 30]

The influence of the temperature and the pH value on activity and selectivity of glucose to gluconic acid oxidation reaction have also been investigated. [33] The temperature range leading to the highest reaction rates was found to be around 50°C at pH 9.5 and 60°C at pH 7.0. The decrease in selectivity of gluconic acid formation at higher temperatures (**Figure 12**) can be explained by the side reactions, which lead to the formation of fructose, mannose, glycoaldehyde, sorbitol and maltose, as described in the reaction network of glucose oxidation (**Figure 13**).
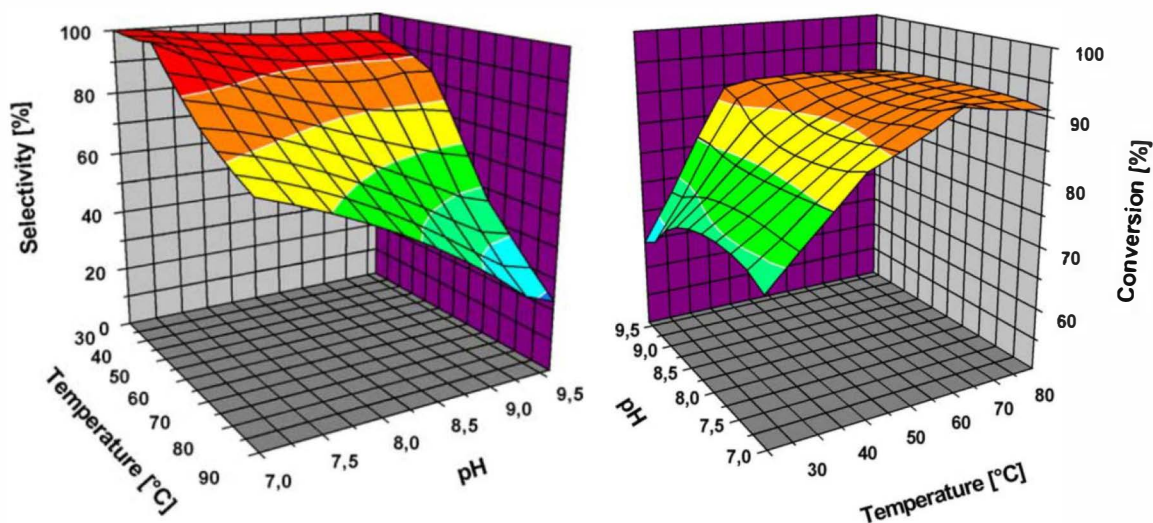

Figure 12. *Selectivity of gluconic acid (left) and conversion of glucose (bottom) at different pH and temerature values.* [33]
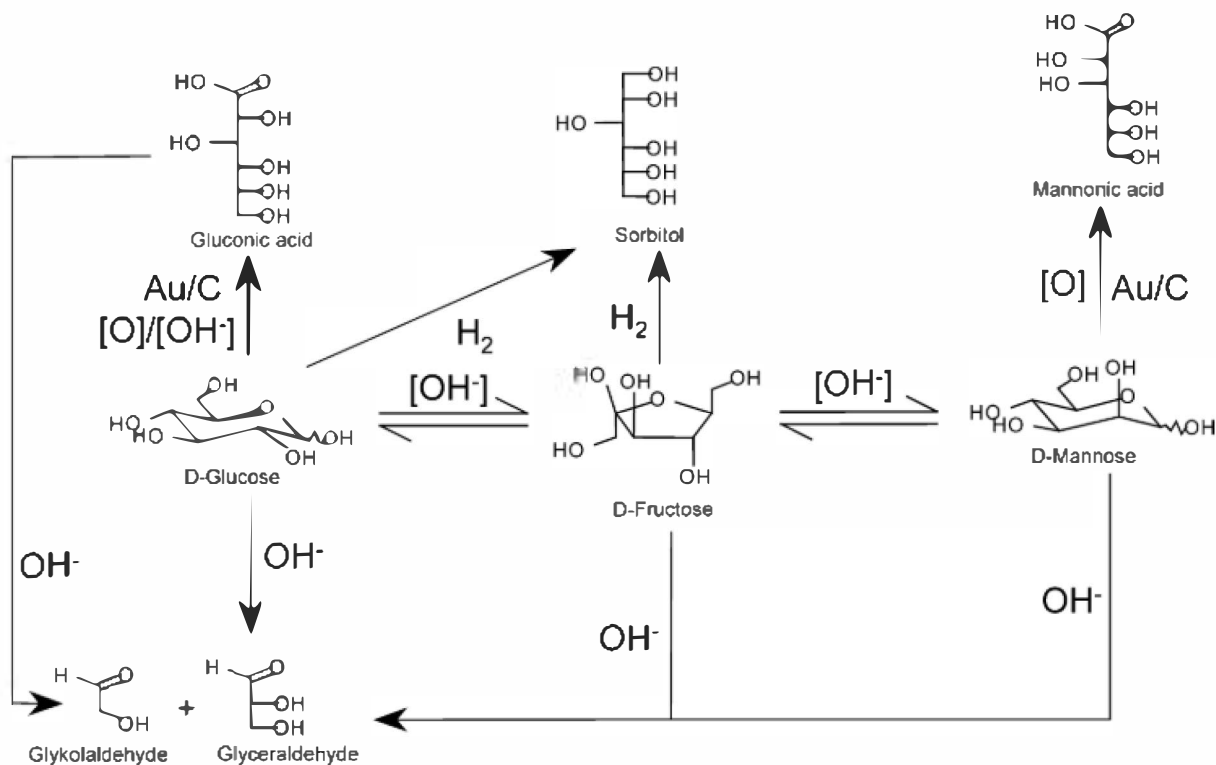
Figure 13. *Reaction network of glucose oxidation reaction in alkaline solution and at higher temperatures.* [33]

Moreover, studies performed by Lama *et al.* showed the significant influence of the surface atomic structure of carbonaceous support materials with comparable pore structure on the catalyst structures and thus their properties for glucose oxidation. Salt-templated porous carbon support with different surface chemistry has been investigated. The rather hydrophobic as-made and hydrogen-treated supports provided higher catalytic activity than hydrophilic supports doped with oxygen and nitrogen.

However, a detailed structure – performance study, concerning the porosity of support material is still missing, and is therefore addressed in this work.

2. Research Goals

In this master thesis, the effect of the pore structure of porous carbon supports on the catalyst structure and on the catalytic activity of heterogeneous gold nanoparticle catalysts for the selective oxidation of D-glucose to D-gluconic acid in aqueous solution with molecular oxygen is investigated.

Traditional oxide supports and nanocarbons have been compared. The oxide supports used in this work are commercially available Aeroxide® TiO_2 P 25, Aeroxide® Alu 130, Aerosil® 380 and self-made ordered mesoporous silica SBA-15. In order to analyze individual factors that supports can contribute to catalytic activity, a commercial carbon material with the comparable porosity, Carbon Black (Vulcan), has been used for a comparison in order to investigate the influence of the chemical nature of the support on the catalysts' properties.

On the other hand, catalysts with highly porous carbonaceous materials as supports have been synthesized with different metal loadings. The capacity of carbons with different pore structures and geometries, as well as morphologies, to maintain high catalytic activity with different gold loadings is investigated. It is a general target in heterogeneous catalysis to maximize the loading of the active component on the support at unchanged catalytic activity per active mater. In this regard, two ordered mesoporous supports (CMK-3 and OMHSTC), microporous carbon aerogel, as well as two commercially available carbons (activated carbon and multiwalled carbon nanotubes (MWCNT)) have been used in order to figure out the ideal pore structure to meet this demand.

Moreover, the adsorption abilities of the catalyst supports employed in this master thesis have been studied through a series of experiments on the adsorption of glucose and gluconic acid.

In order to investigate the dominating mechanism of glucose oxidation reaction under the reaction conditions utilized in this work, a series of catalytic tests have been performed with different catalyst loadings.

3. Results and Discussion

3.1 Influence of the Chemical Structure of the Support Material on Catalytic Activity of the Glucose Oxidation Reaction

3.1.1   Structure of the Catalysts

In this chapter, structures of a series of catalysts supported on oxides have been studied, in comparison to a carbon black material. The selected supports are commercially available Aeroxide® TiO$_2$ P 25 (in further text referred to as titania TiO$_2$ P25), Aerosil® 380 (in further text referred to as silica SiO$_2$ 380), Aeroxide® Alu 130 (in further text referred to as alumina Al$_2$O$_3$ 130, self-made ordered mesoporous silica (SBA-15) and Carbon Black Vulcan. The reason for investigating these supports is their different chemical structures then the one found in carbon materials. For the loading of AuNPs, a method of deposition with a preformed colloidal gold dispersion is used.

Titania TiO$_2$ P25, and its 1 wt. % Au catalyst exhibit almost no internal porosity, but the shape of the N$_2$ physisorption in the area of high relative pressure is indicating external porosity (**Figure 14a**). The latter is the same for all support materials investigated in this chapter.

In the case of alumina Al$_2$O$_3$ 130, and its 1 wt. % Au catalyst, there is slightly higher total uptake of nitrogen, with SSA values ~ 118 m^2/g (**Figure 14b, Table 1**).

Silica SiO$_2$ 380 and its 1 wt. % Au catalyst show much higher porosity than two previously discussed metal oxides, with porosity coming mainly from meso- and macropores (**Figure 14c**). Specific surface area is reaching up to 370 m^2/g and micro- and mesopore volume calculated at p/p$_0$ = 0.95 is ~ 0.9 cm^3/g (**Table 1**).

Vulcan is a carbon black material whose structure and porosity could be compared with the silica support SiO$_2$ 380. SSA value is ~ 390 m^2/g and micro- and mesopore volume calculated at p/p$_0$ = 0.95 is ~ 0.5 cm^3/g (**Table 1**). Similar to silica, negligibly small uptake of nitrogen at low relative pressures is indicating that a material has almost no micropores or narrow mesopores and that the SSA mainly arises from external surface of small individual particles (**Figure 14d**).
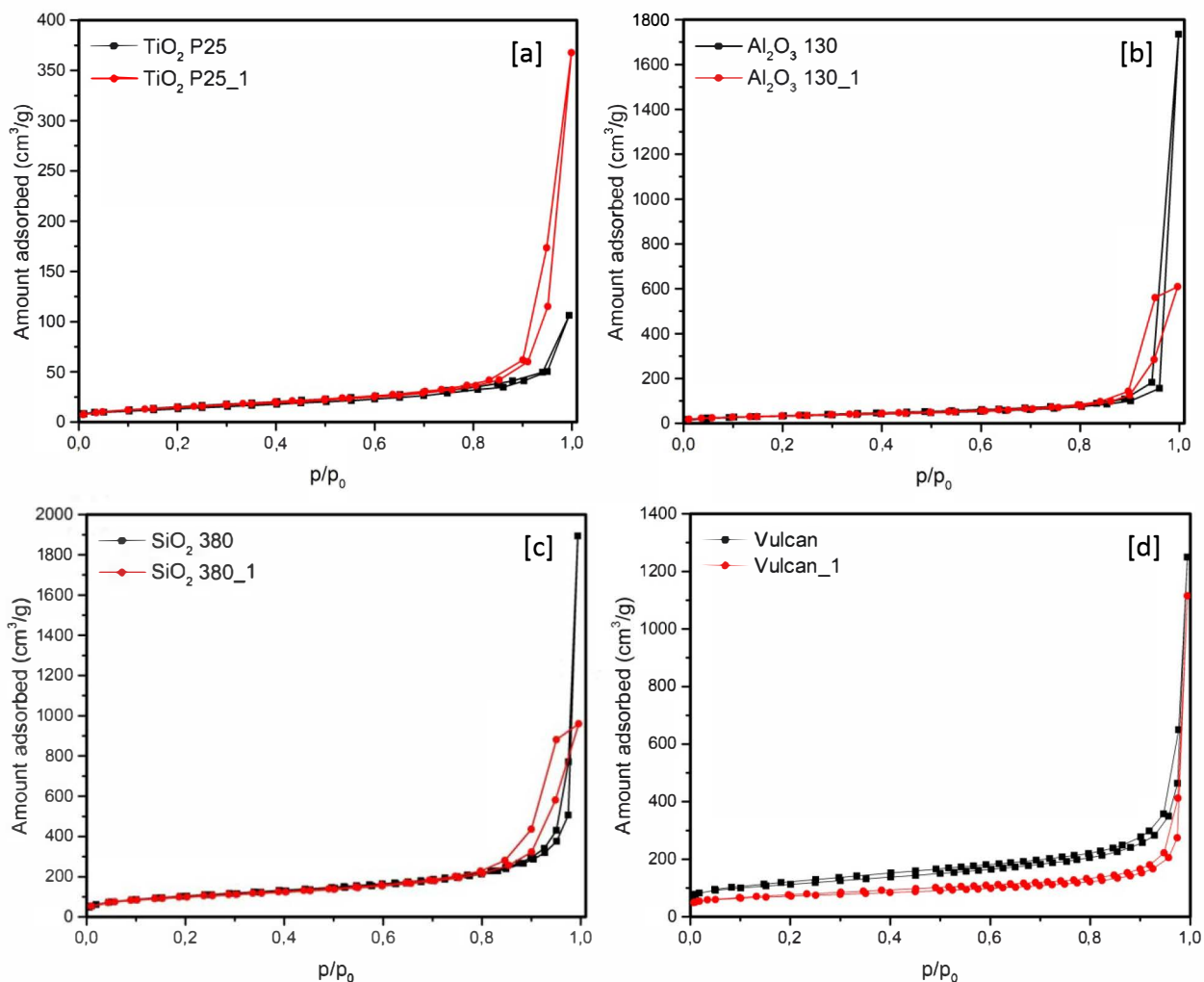
Figure 14. *Nitrogen physisorption (-196 °C) isotherms of TiO₂ P25 [a], Al₂O₃ 130 [b], SiO₂ 380 [c] and Vulcan [d] supports and catalysts.*

Table 1. *Porosity data summary of TiO₂ P25, Al₂O₃ 130, SiO₂ 380 and Vulcan supports and catalysts.*

Sample	SSA_{BET}[a] (m^2/g)	V_{Micro}[b] (cm^3/g)	Average Pore Size (nm)	$V_{Micro + Meso}$[c] (cm^3/g)	Total pore volume (cm^3/g)
TiO₂ P25	47.1	0.004	6.64	0.08	N.A.
TiO₂ P25_1	53.2	0.002	13.39	0.18	N.A.
Al₂O₃ 130	117.1	0.013	8.27	0.24	N.A.
Al₂O₃ 130_1	119.9	0.006	14.68	0.44	N.A.
SiO₂ 380	372.7	0.060	6.25	0.58	N.A.
SiO₂ 380_1	355.7	0.046	10.12	0.90	N.A.
Vulcan	396.6	0.080	7.25	0.54	N.A.
Vulcan_1	249.3	0.060	6.83	0.32	N.A.

[a] Specific surface area calculated using the BET equation ($p/p_0 = 0.05-0.2$).
[b] Micropore volume calculated from the cumulative pore volume up to a diameter of 2 nm (QSDFT method for nitrogen on carbon with slit/cylindrical/spherical pores at -196°C, adsorption branch kernel).
[c] Micro- and mesopore volume calculated at $p/p_0 = 0.95$.

Catalytic reaction of glucose oxidation with molecular oxygen, which is investigated in this study is carried out in aqueous phase. Moreover, the employed method of catalyst synthesis also takes place in aqueous phase. Therefore, interaction of catalyst support materials with water plays an important role in these processes. Different chemical compositions of the oxide supports affect the interaction with water, i.e. surface hydrophilicity/hydrophobicity. Water vapor adsorption isotherms of TiO_2 P25, Al_2O_3 130, SiO_2 380 and Vulcan at 25 °C (**Figure 15**) show that the silica support is slightly less hydrophilic than titania, because it keeps adsorbing water at higher relative pressure and its relative amount of water adsorption is lower. Hydrophilicity of alumina and titania are somewhat comparable, since they both adsorb a relatively large amount of water at at low relative pressure, followed by an additional constant water uptake up to p/p_0 = 0.6-0.9. The strength of interaction with water is also a question of the pore size, therefore it could be concluded that, taking their porosities into consideration (**Table 1**), all these oxide materials exhibit quite hydrophilic behavior. Vulcan, on the other hand, is showing much more hydrophobic character, what can be concluded from negligible uptake at low relative pressures (**Figure 15**). The onset point of water adsorption (a standard indicator for the strength of interaction of water with surfaces) is much higher as compared to the oxidic supports.
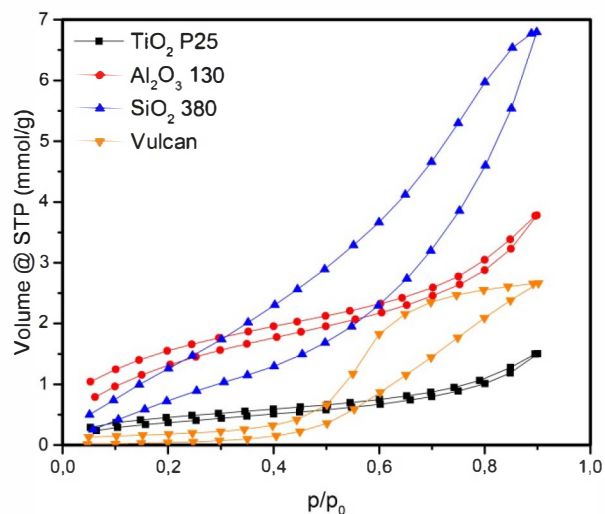

Figure 15. *Water vapour physisorption isotherms (25 ℃) isotherms of TiO₂ P25, Al₂O₃ 130, SiO₂ 380 and Vulcan catalysts.*

Titania-supported catalyst TEM images are showing interconnected metal oxide (TiO_2) particles of near-spherical shape, with small number of relatively well-dispersed small AuNPs (**Figure 16**). The total amount of gold loaded on this support as determined by ICP measurements, is 0.28

wt. % (**Table 1**). In addition, although taken TEM images did not provide enough gold particles for an accurate particle size distribution, **Figure 16** shows small AuNPs, with average size of approximately 4 nm. It may be concluded that TiO_2 P25 support is providing a good stabilization of gold nanoparticles, however the low porosity of this support is preventing a larger number of AuNPs from depositing on its surface.

In the case of alumina, a slightly higher porosity of this support, in comparison to titania, had an effect on metal loading, with 0.53 wt. % gold in Al_2O_3 130_1 catalyst. The morphology of this support is probably giving more available anchoring sites for gold particles then TiO_2 P25, which can be observed in **Figure 16**.

Silicon dioxide supports whose structure and effect on catalytic activity were investigated in this work were SiO_2 380 and SBA-15. Even though similar in chemical composition, these two materials present notably different structure and morphology (**Figure 16**). SiO_2 380_1 shows completely amorphous and disordered material, with very few visible AuNPs. ICP data supports the assumption of low metal loading, showing 0.31 wt. % of gold (**Table 1**). TEM images of SBA-15_1 (**Figure 16**) display ordered arrays of mesopores, with almost no observable AuNPs. The total gold loading obtained through ICP was below 0.1 wt. % (**Table 1**).

On the contrary, amorphous carbonaceous support Vulcan, with moderate porosity comparable to SiO_2 380, has areas with high number of small AuNPs (**Figure 16**). From this set of catalysts, Vulcan_1 was the only sample where particle size distribution could provide statistically relevant information. This carbon showed good stabilization of nanoparticles, with narrow PSD and average AuNP size of 3.88 nm (**Figure 16**, **Table 1**). Despite the fact that the area available for the deposition of gold nanoparticles is similar, Vulcan_1 shows higher Au loading of 0.4 wt. % (**Table 1**). It could be deduced that the affinity of gold towards carbon is higher than towards oxide supports. This is likely due to the fact that the citrate-stabilized gold nanoparticles exchange their ligands more rapidly against carbon than against oxidic materials and thus the gold deposition is more rapid on this support. During gold deposition it could be observed that in the case of all oxide supports, the red color of the dispersion, indicating the presence of AuNPs, is fading much slower than in the case of carbon supports. Moreover, the dispersion remained light-red in all cases of oxide supports, even after vigorous stirring and ultrasonic treatment, which confirms the abovementioned conclusion on the affinity of gold towards these supports.
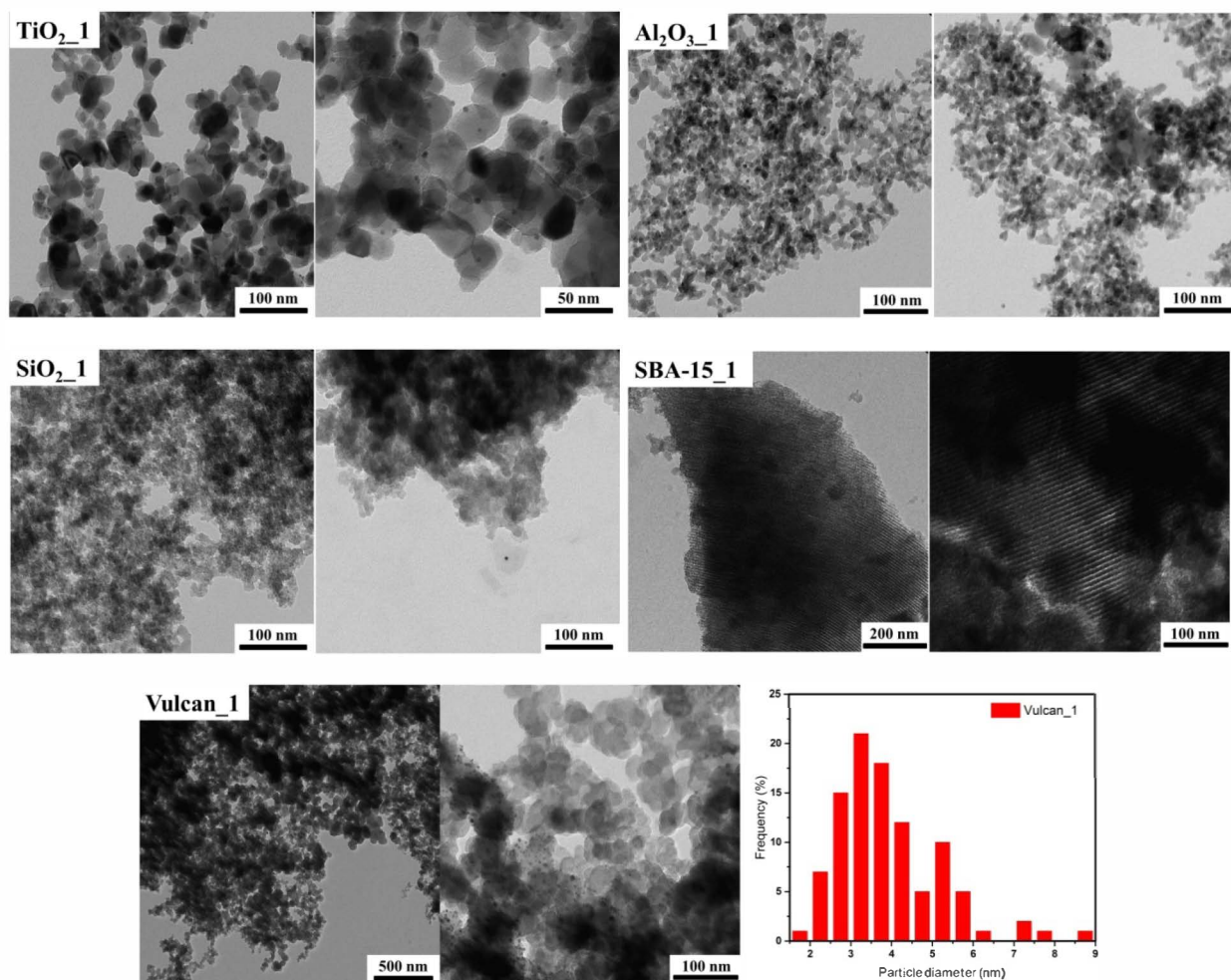
Figure 16. *TEM images of the catalysts TiO₂_1, Al₂O₃_1, SiO₂_1, SBA-15_1, Vulcan_,1 and the corresponding Au particle size distribution for Vulcan_1. *Particle size distributions were not calculated for this series of catalysts (except for Vulcan_1), because of the insufficient number of particles obtained from the TEM images.*

3.1.2 Catalytic Activity

The catalytic activity of the selected catalysts for the glucose oxidation reaction is tested for 50 mg of catalyst in 50 mL of glucose solution (0.1 mol/dm³), on 45°C with stirring of 800 rpm. The solution is bubbled with oxygen (250 mL/min), and the pH value is kept at 9. The reaction is followed by titration with sodium hydroxide (1 mol/dm³), therefore the volume of added NaOH vs. time is plotted in the graph (**Figure 17**). The selectivity of the catalysts is estimated by analyzing the products of reaction by high performance liquid chromatography, which in the cases of full conversion resulted in total selectivity towards gluconic acid.

In **Figure 17** and **Table 2**, the results of glucose oxidation reaction with above described catalysts are shown. Both silica-supported catalysts showed no activity for this reaction, which could be attributed to several factors. Firstly, low loading of active phase, as seen in **Table 2**. Furthermore, it is also possible that available Au species is not in its catalytically active metallic form, due to the interaction of silicon dioxide with the metal. By using ordered mesoporous silica support with high surface area[67], the importance of chemical structure of the support is even more pronounced. Namely, the provided higher surface area did not lead to higher catalytic activity. Al_2O_3 130_1 is the catalyst that has resulted in highest amount of gold (0.53 wt. %), despite having a low porosity (**Table 1**). Nonetheless, metal-time yield of this catalyst was moderately low. This may be due to the agglomeration of gold, and the incapability of alumina to stabilize small nanoparticles.

TiO_2 P25_1 gave the best performance among oxide supports, albeit having the lowest porosity and available surface for gold to be deposited (**Table 1**). This may be attributed to the stabilization of gold clusters by the titania lattice oxygen, forming Au–O–Ti bonding. These AuNPs anchored on TiO_2 are showing good catalytic performance, but the essential drawback of using titania as a catalytic support is its hardly-tackled low porosity, which also lead to low metal loading.

The nature of carbonaceous supports is providing weak interaction with metal nanoparticles, therefore even the catalyst with relatively low surface area in comparison to other carbon catalysts (Vulcan_1) is still proven to be more active than oxide-supported catalysts.

In conclusion, the surface chemistry of the oxide supports, namely their hydrophilicity and possible strong interaction with gold nanoparticles, is the reason for their low catalytic activity.
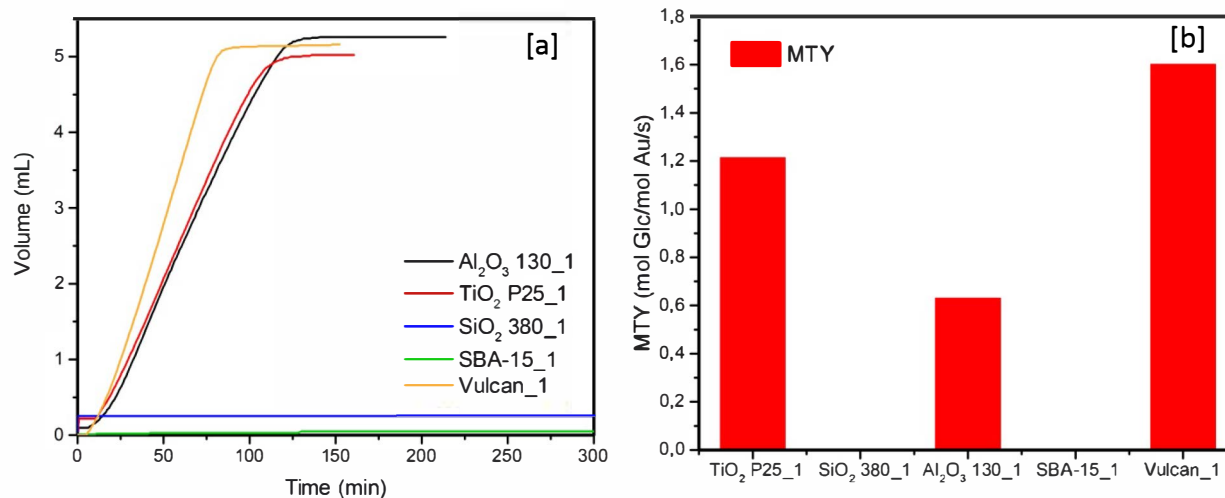
Figure 17. *Volume of added NaOH – time diagrams for the reaction of glucose oxidation using mentioned catalysts [a] and corresponding metal-time yield [b].*

Table 2. *ICP data summary, average Au particle sizes and gold-specific activity (expressed as metal-time yield, MTY) of the investigated catalysts.*

Catalyst	Au (wt. %)$_{ICP}$	PSD (nm)	MTY (mol Glc/mol Au/s)
TiO$_2$_1	0.28	N.A.	1.21
Al$_2$O$_3$_1	0.53	N.A.	0.63
SiO$_2$_1	0.31	N.A.	No conversion
SBA-15_1	0.04	N.A.	No conversion
Vulcan_1	0.40	3.88 ± 1.25	1.60

3.2 Pore Structure – Performance Relationship on the Catalytic Glucose Oxidation Reaction

3.2.1 Structure of the Catalysts Supported on Carbonaceous Supports

For the purpose of investigating different pore structure of carbon supports, as well as the effect of different AuNP loading, two ordered mesoporous supports (CMK-3 and OMHSTC), microporous carbon aerogel, as well as two commercially available carbons (activated carbon and MWCNT) have been employed. In this chapter, the structures of carbon supports and the corresponding catalysts with targeted loadings of 0.5 wt. %, 1 wt. % and 5 wt. % have been studied. For the loading of AuNPs, a method of deposition with a preformed colloidal gold dispersion is used.

N_2 (−196 °C) physisorption experiments were carried out to quantify the pore structures of prepared catalysts, and the corresponding carbon supports (**Figure 18 – 24**). Isotherms of activated carbon (AC) alone and its catalysts (**Figure 18**) show no significant difference in porosity. In other words, deposition of gold nanoparticles seems to take place only on the external surface of this carbon with rather the characteristics of a physical mixture than a real nanocomposite. The total uptake of N_2 is moderate, with total pore volumes (V_t) around 0.7 cm^3/g (**Table 3**), however in the microporous area nitrogen uptake is noticeable ($V_{Micro} \sim 0.27$ cm^3/g). Although the adsorption is happening over the entire range of relative pressures, the shape of the isotherms is pointing out that AC's surface area is mainly resulting from micropores. The pore size distribution for this type of carbon and the corresponding catalysts is relatively broad due to the ill-defined pore structure of activated carbon materials (**Figure 18b** and **c**).
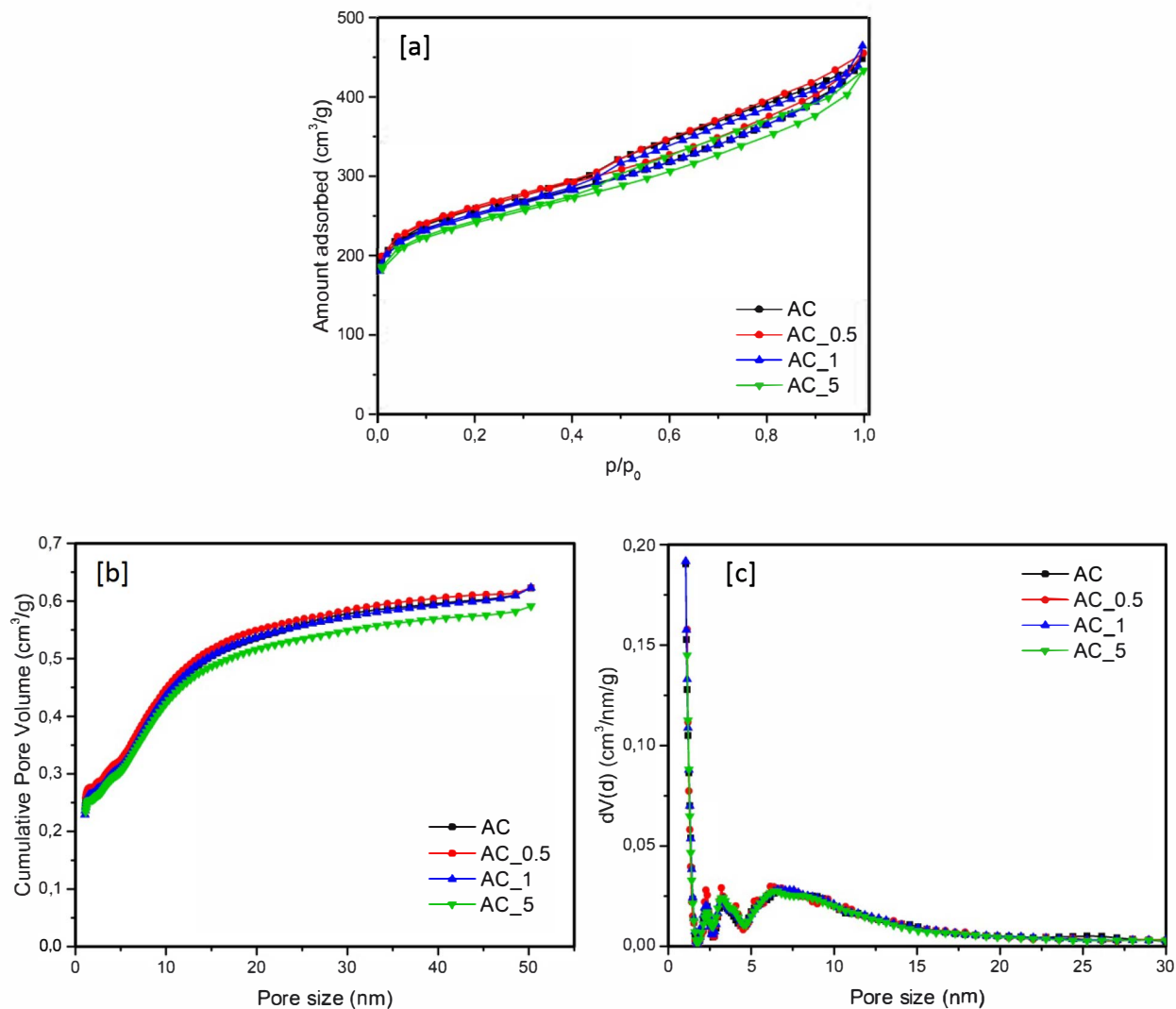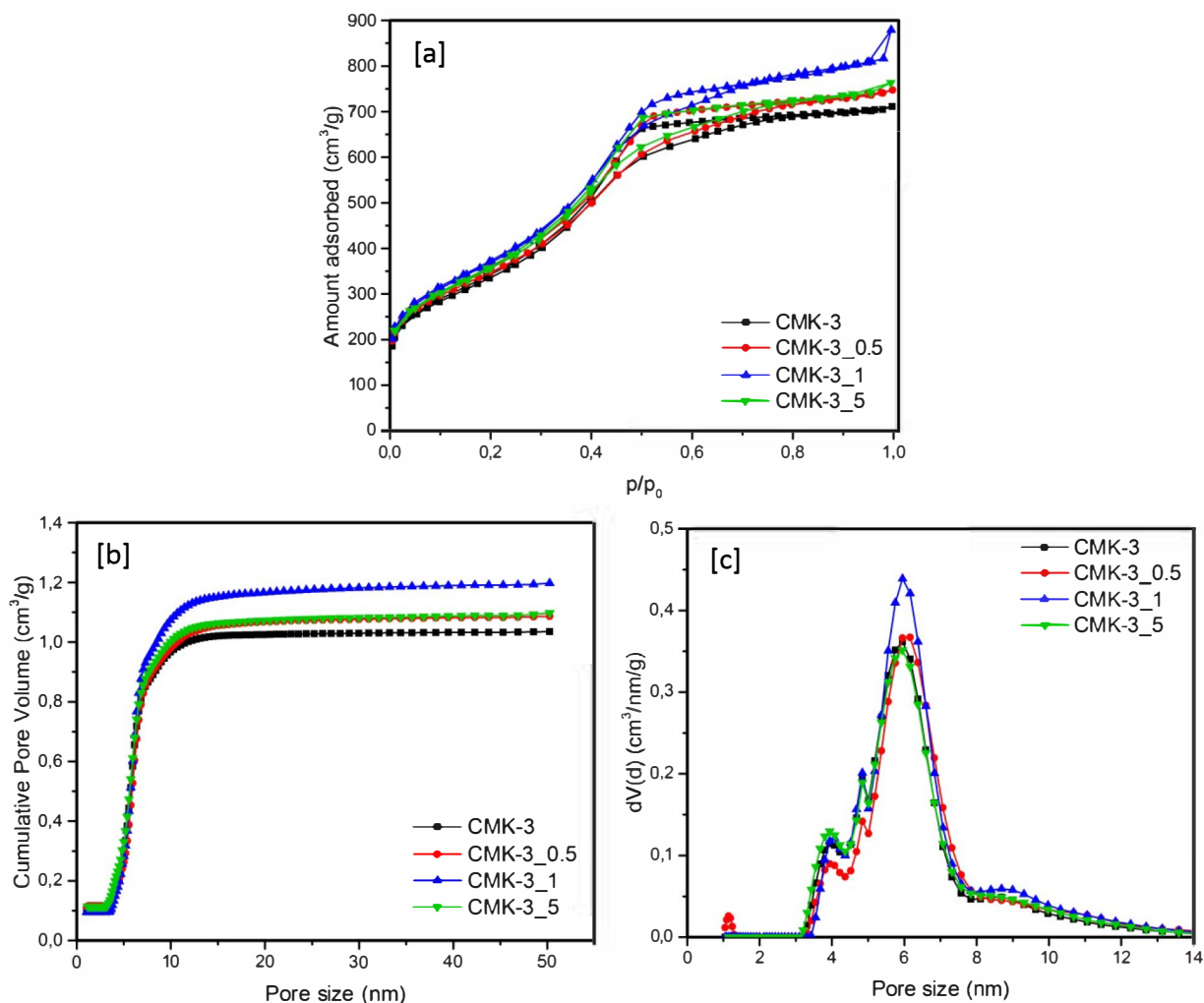
Figure 18. *Nitrogen physisorption (-196 ℃) isotherms of activated carbon catalysts and the pristine AC support [a], corresponding cumulative QSDFT (nitrogen on carbon with slit/cylindrical/spherical pores at -196 ℃, adsorption branch kernel) pore size distribution [b] and differential QSDFT PSD [c].*

Table 3. *Porosity data summary of activated carbon catalysts.*

Sample	SSA$_{BET}$[a] (m^2/g)	V$_{Micro}$[b] (cm^3/g)	Average Pore Size (nm)	Total pore volume (cm^3/g)
AC	866.6	0.28	3.29	0.71
AC_0.5	920.3	0.28	3.07	0.71
AC_1	835.7	0.27	3.45	0.72
AC_5	830.8	0.26	3.24	0.67

[a] Specific surface area calculated using the BET equation (p/p$_0$ = 0.05-0.2).
[b] Micropore volume calculated from the cumulative pore volume up to a diameter of 2 nm (QSDFT method for nitrogen on carbon with slit/cylindrical/spherical pores at -196°C, adsorption branch kernel).

CMK-3 support and catalysts also do not exhibit significantly different porosities (**Figure 19a**). They provide specific surface areas above 1200 m^2/g and total pore volumes of ~ 1.2 cm^3/g (**Table 4**). CMK-3 and the corresponding catalysts show a hysteresis loop at $p/p_0 = 0.4$-0.7, as it is typical for materials with hexagonal ordered mesopores. CMK-3 is mainly mesoporous as indicated by the small contribution of micropores to the total pore volume (**Figure 19b**). It exhibits a low micropore volume of ~ 0.1 cm^3/g, which is mostly caused by the random surface defects and within the carbon nanorods, related to the decomposition of the carbon precursor. At higher relative pressures, CMK-3 shows high uptake due to the complete filling of the mesopores with nitrogen. Pore size distribution was further analyzed using the quenched solid density functional theory (QSDFT) for N_2 adsorbed on carbon with slit/cylindrical pore shape (**Figure 19c**) and it is concluded that CMK-3 retain a narrow PSD with sharp maxima in the narrow mesopore range due to its more ordered mesopore system in comparison to activated carbon with a random arrangement of mesopores.

Figure 19. *Nitrogen physisorption (-196 ℃) isotherms of CMK-3 catalysts and the pristine CMK-3 support [a], corresponding cumulative QSDFT (nitrogen on carbon with slit/cylindrical/spherical pores at -196 ℃, adsorption branch kernel) pore size distribution [b] and differential QSDFT PSD [c].*

Table 4. *Porosity data summary of CMK-3 catalysts.*

Sample	SSA_{BET}[a] (m^2/g)	V_{Micro}[b] (cm^3/g)	Average Pore Size (nm)	Total pore volume (cm^3/g)
CMK-3	1208.0	0.09	3.65	1.10
CMK-3_0.5	1247.7	0.11	3.72	1.16
CMK-3_1	1327.5	0.09	4.11	1.36
CMK-3_5	1276.8	0.11	3.70	1.18

[a] Specific surface area calculated using the BET equation ($p/p_0 = 0.05-0.2$).
[b] Micropore volume calculated from the cumulative pore volume up to a diameter of 2 nm (QSDFT method for nitrogen on carbon with slit/cylindrical/spherical pores at -196°C, adsorption branch kernel).

The ordered arrangement of the carbon nanorods in CMK-3 gives rise to the small-angle X-ray scattering (SAXS) peaks (**Figure 21**), which can be assigned to (100), (110), and (200) diffractions of the 2-d hexagonal space group (*p6mm*). Well-resolved (100) peak locate at $2\theta =$ 1.17°.

OMHSTC, and the catalysts with this support exhibit type IV(a) isotherms with a continuous slope above a relative pressure of 0.2, and a hysteresis loop in the relative pressure range between 0.5 and 0.9 (**Figure 20a**). Thus, the existence of well-defined mesopores in these carbons is evident. The amount of micropores is slightly increased in comparison to CMK-3 (0.13-0.17 cm^3/g) (**Table 5**) resulting from the addition of ZnCl$_2$ salt template. However, from QSDFT PSD (**Figure 20c**), it is apparent that the average pore size is larger than in the case of CMK-3, despite the fact that they are both synthesized using SBA-15 as hard template. This can be ascribed to the formation of a surface layer of ZnCl$_2$ inside the nanochannels of SBA-15 (**Figure 22**). During the impregnation step, Lewis acidic Zn^{2+} ions interact with the pore walls of the negatively charged, electron lone-pair-rich SBA-15. Therefore, the salt template distributes along the channel and only partially distributes inside the carbon precursor into the channels of the silica. This causes the growth of the mesopores between the cylindrical carbon rods after the removal of SBA-15 and the salt template, particularly the mesopore size of the carbon is a sum of the size of the pore walls of SBA-15 and two times the thickness of the salt layer. [53]

In small-angle X-ray scattering (SAXS) measurements (**Figure 21**), OMHTC shows a well-resolved peak assigned to (100) diffractions of the 2-d hexagonal space group (*p6mm*), which is located at $2\theta = 1.12°$. This is an indication that a distance between the centers of carbon nanorods is larger than in CMK-3 ($2\theta = 1.17°$). This is likely because ZnCl$_2$ (until its evaporation) stabilizes the hard template SBA-15 and provides resistance against shrinkage during high-temperature treatment, which is a known effect for sol–gel derived silicas. The cumulative PSD plots (**Figure 20b**) indicate that the micropores only contribute a small fraction of the total pore volume in the OMHSTC.
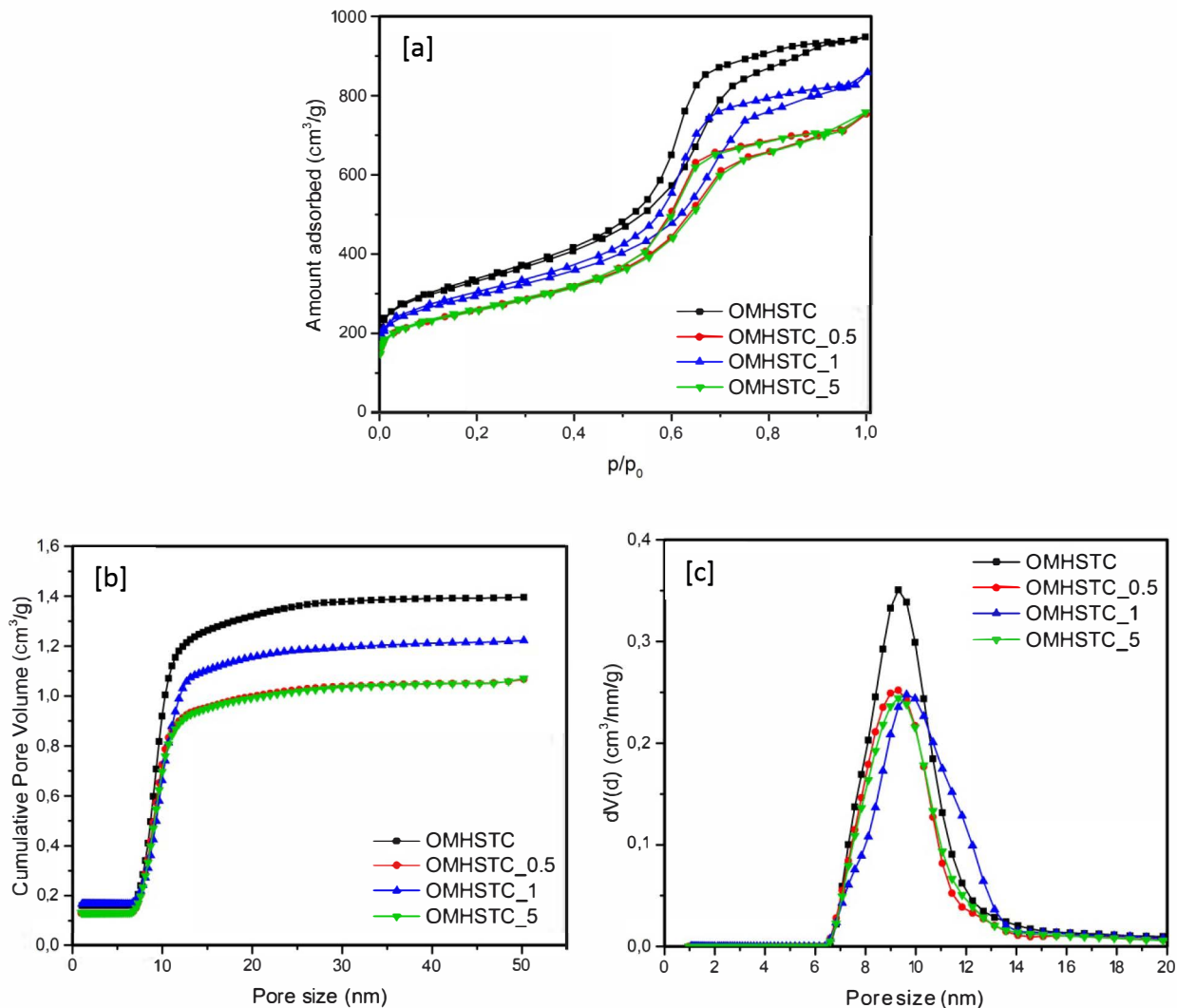
Figure 20. *Nitrogen physisorption (-196 °C) isotherms of OMHSTC catalysts and the pristine OMHSTC [a], corresponding cumulative QSDFT (nitrogen on carbon with slit/cylindrical/spherical pores at -196 °C, adsorption branch kernel) pore size distribution [b] and differential QSDFT PSD [c].*

Table 5. *Porosity data summary of OMHSTC catalysts.*

Sample	SSA$_{BET}$[a] (m^2/g)	V$_{Micro}$[b] (cm^3/g)	Average Pore Size (nm)	Total pore volume (cm^3/g)
OMHSTC	1164.2	0.16	5.05	1.47
OMHSTC_0.5	901.4	0.13	5.18	1.17
OMHSTC_1	1037.4	0.17	4.93	1.28
OMHSTC_5	898.8	0.13	5.23	1.17

[a] Specific surface area calculated using the BET equation (p/p$_0$ = 0.05-0.2).
[b] Micropore volume calculated from the cumulative pore volume up to a diameter of 2 nm (QSDFT method for nitrogen on carbon with slit/cylindrical/spherical pores at -196°C, adsorption branch kernel).
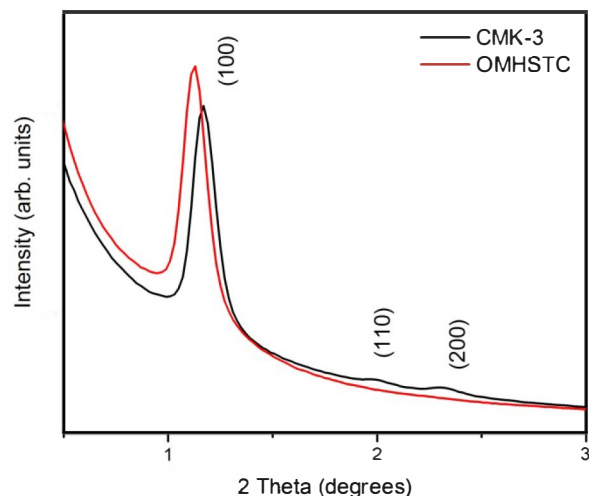
Figure 21. *SAXS patterns of CMK-3 and OMHSTC.*
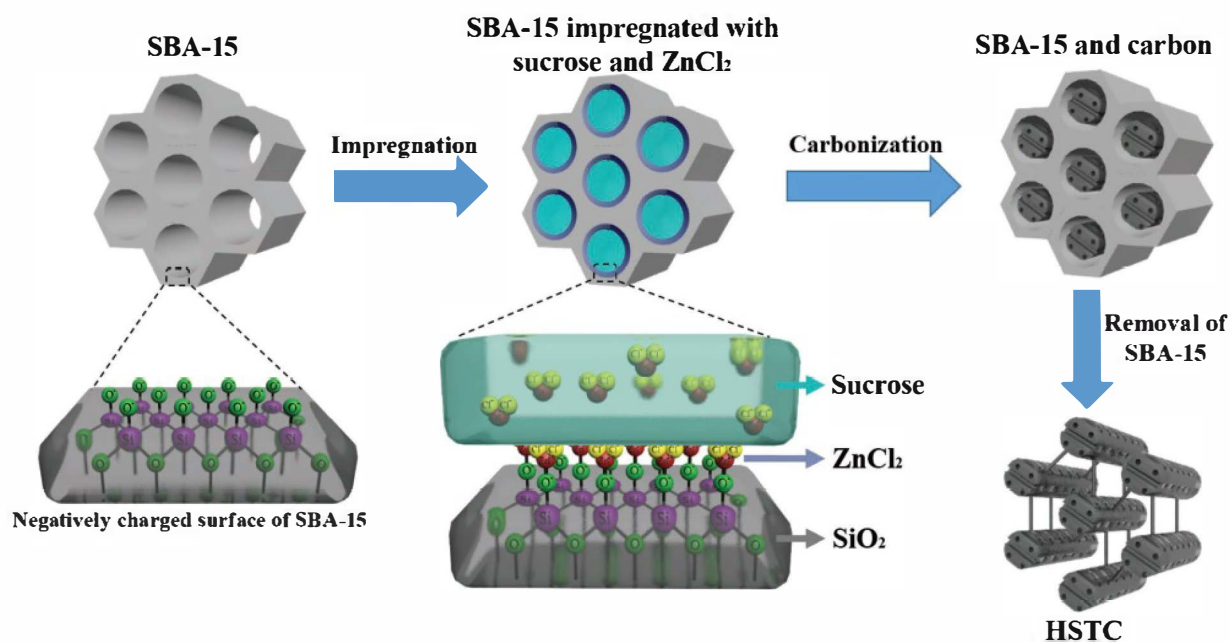
Figure 22. *Possible mechanism of enlargement of mesopore size in OMHSTC caused by salt templating.* [53]

MWCNT and the corresponding catalysts generally show almost no internal porosity (SSA ~ 12 m^2/g, $V_{Micro + Meso}$ ~ 0.03 cm^3/g) (**Figure 23a**, **Table 6**). The shape of the isotherm in the area of high relative pressures (p/p_0 > 0.95) is indicating external meso- and macro porosity, resulting from the voids created from the carbon nanotube network. Constant nitrogen uptakes along the entire range of pressures are related to the broad PSD of the MWCNTs (**Figure 23b** and **c**).

31
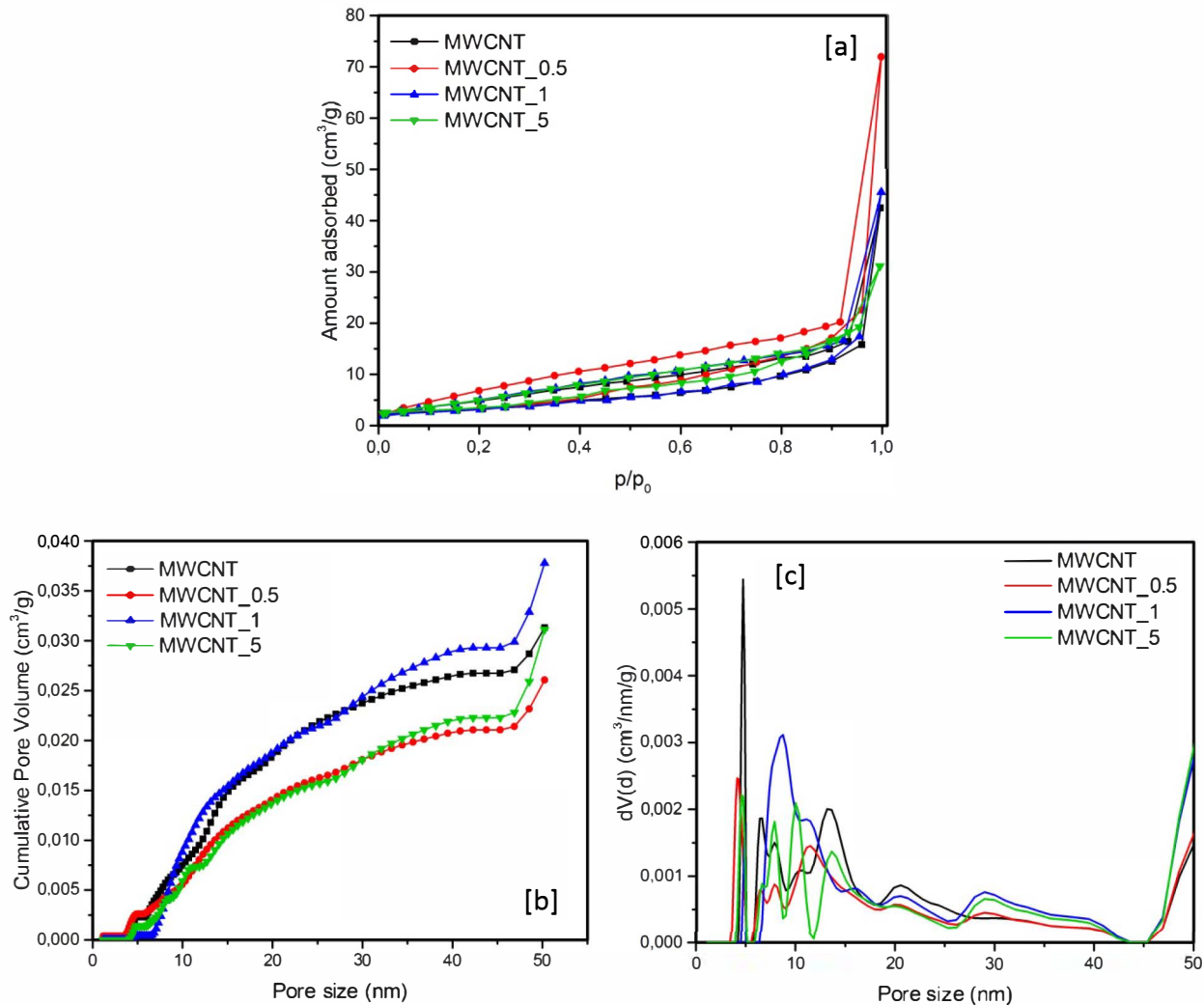
Figure 23. *Nitrogen physisorption (-196 ℃) isotherms of MWCNT catalysts and the pristine MWCNT support [a], corresponding cumulative QSDFT (nitrogen on carbon with slit/cylindrical/spherical pores at -196 ℃, adsorption branch kernel) pore size distribution [b] and differential QSDFT PSD [c].*

Table 6. *Porosity data summary of MWCNT catalysts.*

Sample	SSA$_{BET}$[a] (m^2/g)	V$_{Micro}$[b] (cm^3/g)	Average Pore Size (nm)	V$_{Micro + Meso}$[c] (cm^3/g)
MWCNT	12.3	N.A.	9.63	0.03
MWCNT_0.5	11.4	N.A.	8.59	0.02
MWCNT_1	12.0	N.A.	11.7	0.03
MWCNT_5	11.3	N.A.	9.55	0.03

[a] Specific surface area calculated using the BET equation (p/p$_0$ = 0.05-0.2).
[b] Not applicable for this series of catalysts – no microporosity.
[c] Micro- and mesopore volume calculated at p/p$_0$ = 0.95.

In the case of the carbon aerogel support, the catalyst synthesis was performed only with 1 and 5 wt. % of Au, due to the limited amount of available material. The nitrogen physisorption

isotherms shows the shape that is typical for the open-cell aerogel-type pore structure (**Figure 24a**). The high uptake of nitrogen at p/p₀ > 0.95 is associated with the filling of the large meso- and macropores, which are responsible for the very high pore volumes. With both Aerogel_1 and Aerogel_5, there is a large number of micropores, namely ~ 0.5 cm³/g and ~ 0.3 cm³/g, respectively (**Table 7**). The large SSA of these materials is mostly related to the open-cell foam morphology consisting of interconnected nm-sized primary particles as well as to the presence of abundant micropores. Here, the existence of micropores smaller than 1 nm can also be observed from pore size distribution diagrams (**Figure 24b** and **c**). Since the isotherms do not reach a plateau and the amount of adsorbed gas at high relative pressure can be largely influenced by minor temperature variations, the total pore volume was not calculated using N₂ physisorption.
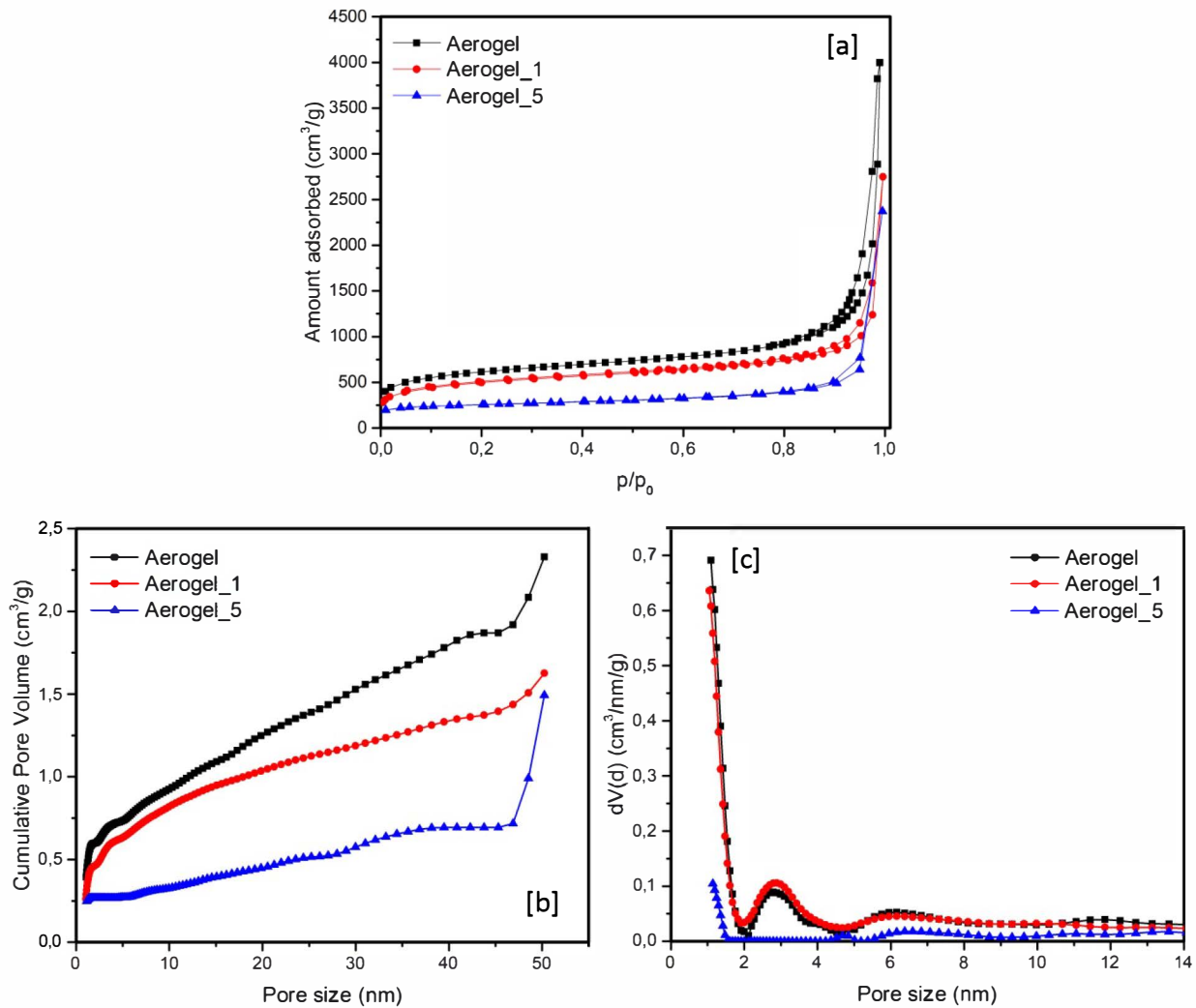
Figure 24. *Nitrogen physisorption (-196 °C) isotherms of Aerogel catalysts and the pristine Aerogel support [a], corresponding cumulative QSDFT (nitrogen on carbon with slit/cylindrical/spherical pores at -196 °C, adsorption branch kernel) pore size distribution [b] and differential QSDFT PSD [c].*

Table 7. *Porosity data summary of Aerogel catalysts.*

Sample	SSA$_{BET}$[a] (m^2/g)	V$_{Micro}$[b] (cm^3/g)	Average Pore Size (nm)	V$_{Micro + Meso}$[c] (cm^3/g)
Aerogel	2149.8	0.59	4.25	2.28
Aerogel_1	1763.6	0.46	3.55	1.56
Aerogel_5	871.6	0.26	4.55	0.99

[a] Specific surface area calculated using the BET equation (p/p$_0$ = 0.05-0.2).
[b] Micropore volume calculated from the cumulative pore volume up to a diameter of 2 nm (QSDFT method for nitrogen on carbon with slit/cylindrical/spherical pores at -196°C, adsorption branch kernel).
[c] Micro- and mesopore volume calculated at p/p$_0$ = 0.95.

In the TEM images of the set of catalysts supported on AC, it is observed that, although not providing large SSA, it is possible to deposit quite large amount of AuNP on their surface (**Figure 25**, **Table 8**). Theoretical loading of gold of 0.5 wt. % yielded in 0.17 wt. % gold deposited, with an average particle size of 9.5 nm. The TEM images show that, although large in size, nanoparticles have large distances between them (**Figure 25 (top)**). Moreover, it is assumed that, since this carbon is mainly microporous, the AuNPs are located only on the external surface of the carbon particles. For the AC_1, the gold loading was 0.47 wt. %, meaning that half of the targeted loading of the metal nanoparticles from the colloidal suspension was achieved on the support. There are several possible reasons behind such a notable difference between the targeted metal loading and the one obtained from ICP measurements. Firstly, possible high error of ICP measurements, together with sample preparation which includes burning off the carbon. Secondly, potential water adsorbed on the surface and in the pores of carbon supports may be the cause of error during the weighing step of catalyst preparation. Finally, a hydrate of tetrachloroauric acid, which is a gold precursor used, may contain more water than expected, again leading to inaccuracy in targeted gold loading. Nonetheless, the red color of AuNP dispersion disappeared in all cases of carbon-supported catalysts. Hence, it can be assumed that the gold loading is relatively comparable to the targeted loading, and is only affected by unknown water content of gold precursor. PSD of AC_1 is narrower than in previous case, and the average particle size is notably smaller, 4.4 nm (**Figure 25 (middle)**, **Table 8**). However, these small AuNPs are deposited quite close to each other. In the case of AC_5, less than one-fifth of available gold in dispersion was deposited on the surface – 0.9 wt. % (**Table 8**). The average size of the nanoparticles is 7.6 nm, and they are positioned in very close proximity (**Figure 25 (bottom)**).
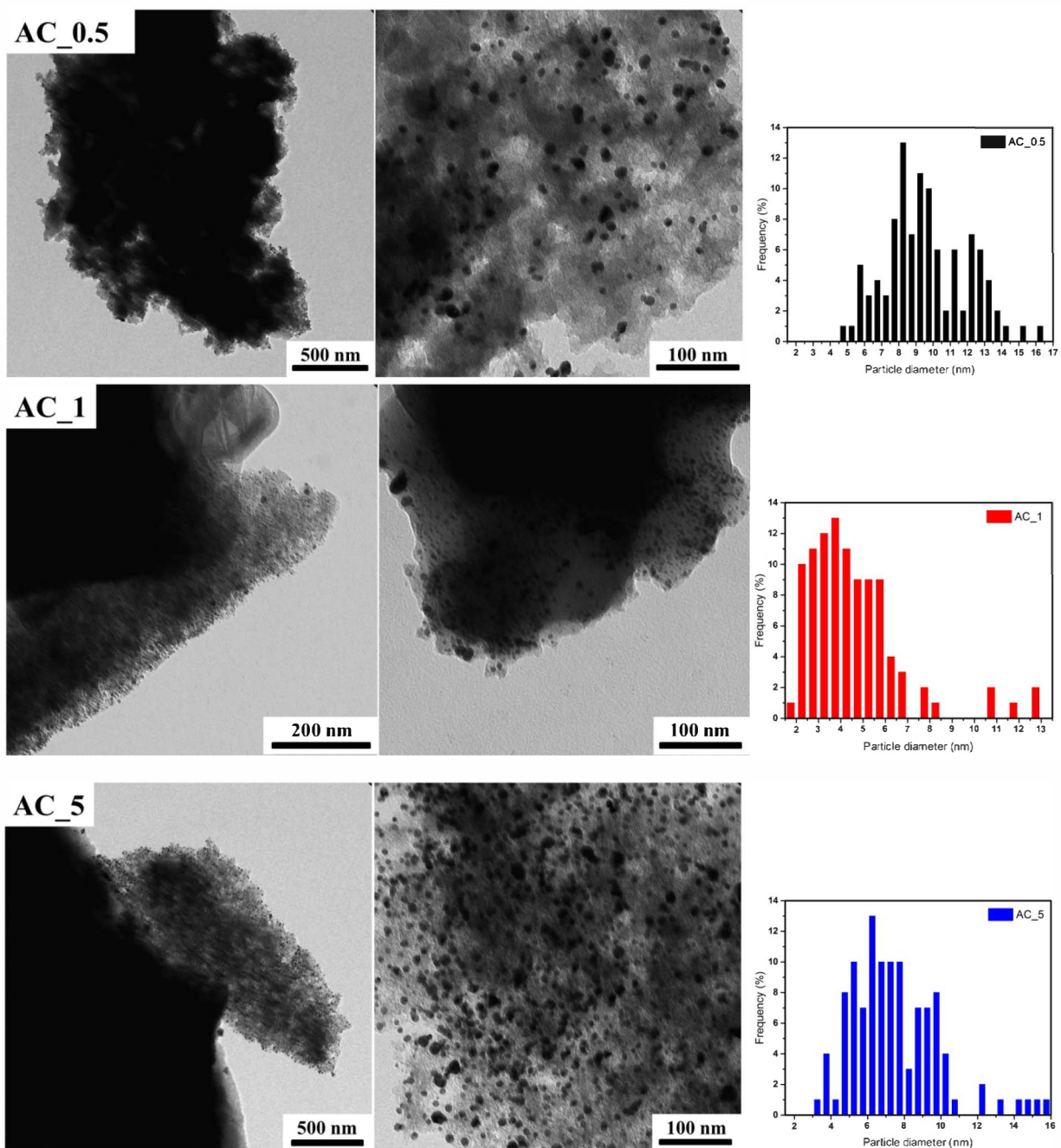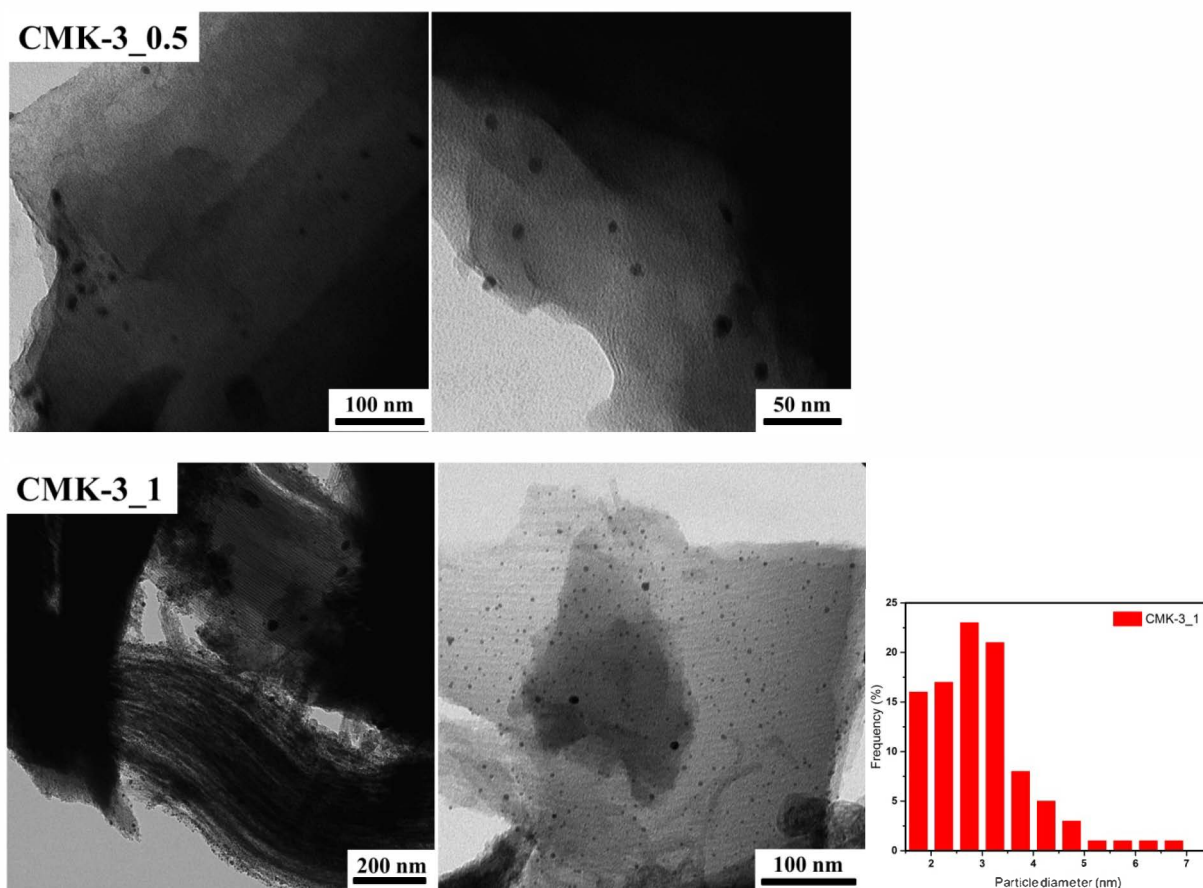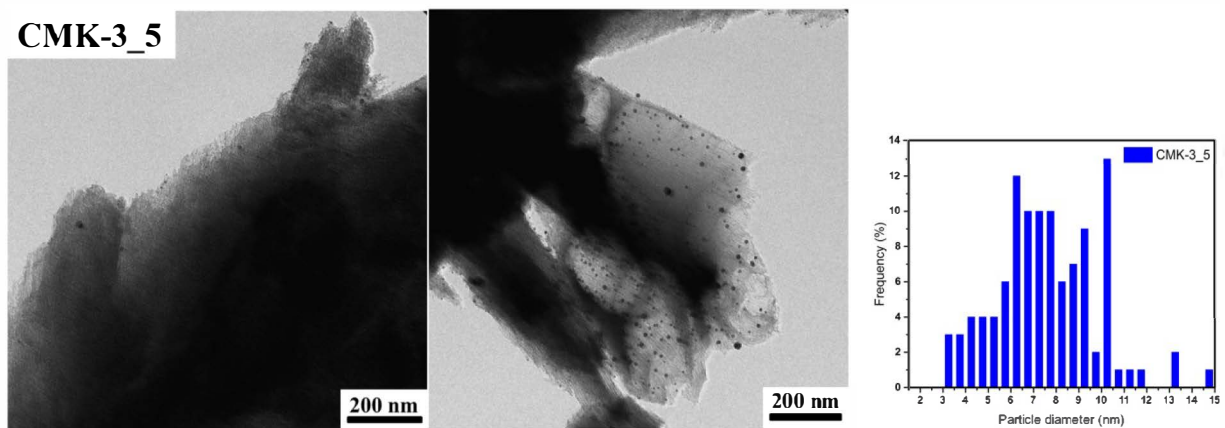
Figure 25. *TEM images of the catalysts AC_0.5 (top), AC_1 (middle), AC_5 (bottom) and the corresponding Au particle size distributions.*

Since only 0.15 wt. % is deposited on it (**Table 8**), CMK-3_0.5 TEM images did not present enough of the visible particles in order to conduct a statistically relevant PSD calculation (**Figure 26 (top)**). Nevertheless, what could be observed from the given images is that middle-in-size, AuNPs on this carbon are well distanced from each other. In the case of CMK-3_1, mesoporous ordered nanorods are clearly observable (**Figure 26 (middle)**). 0.27 wt. % of gold deposited on

35

this carbon has a very narrow particle size distribution, with average size of 4.0 nm (**Figure 26 (middle)**, **Table 8**). Furthermore, it is assumed that mesoporous system of this carbon support is providing area for deposition of gold. However, occurrence of agglomerated particles of gold, larger than the diameter of hollow carbonaceous pores, is indicating that clearly not all of the AuNPs in this catalyst are inside of the mesopores, rather also on the external surface. 0.52 wt. % of gold has been detected in CMK-3_5 (**Table 8**). Concluding from average particle size (7.7 nm) and its broad PSD (**Figure 26 (bottom)**), it is apparent that much smaller part of AuNP can be embedded within the mesoporous system and the larger part rather agglomerates on the external surface of CMK-3 particles.

Figure 26. *TEM images of the catalysts CMK-3_0.5 (top), CMK-3_1 (middle), CMK-3_5 (bottom) and the corresponding Au particle size distributions. *CMK-3_0.5 was excluded from calculation of particle size distribution, because of the insufficient number of particles obtained from the TEM images.*

OMHSTC catalysts all exhibit small gold particles, with narrow PSDs (4.0 nm for OMHSTC_0.5, 3.4 nm for OMHSTC_1 and 4.4 nm for OMHSTC_5) (**Figure 27**, **Table 8**). As in the case of CMK-3, it is expected that this ordered mesoporous support provides space in its mesopores for gold deposition to take place. OMHSTC_0.5 has particles well distanced from each other, while in the case of OMHSTC_1, they seem to be a bit closer. OMHSTC_5 displays more gold agglomerations than the other two catalysts on the same support, however the average particle size is still comparably small. It has to be noted, that this carbon support yielded in the highest percentage of gold deposited (2.99 wt. % for OMHSTC_5) among all of the tested carbonaceous and oxide supports (**Table 8**). What seems to be the case for both CMK-3 and OMHSTC is that with smaller gold loadings, mesoporosity is used more, whereas with higher loadings, the gold gets distributed over the external surface of carbon particles. Furthermore, data obtained by nitrogen physisorption are indicating that the pores of these materials do not get significantly clogged (**Figure 19**, **Figure 20**). From this, it can be concluded that probably when carbon gets in contact with the colloidal gold dispersion, deposition is first happening inside of the mesoporous nanorods. However, since the affinity of carbon towards gold is high, the particles are not migrating too deep into the mesopores, but they interact with the carbon rapidly, which results in particles deposited close to the entrance of the pore. In addition, it has to be taken into consideration that AuNP is stabilized by citrate molecules, which makes these particles larger in diameter, as well as negatively charged. Analogous to organometallic complexation chemistry, the ligand exchange mechanism between citrate ligand and carbon support happens

quite quick, so the migration depth of metallic particles is limited due to strong anchoring. The advantage of OMHSTC over CMK-3 is its larger mesopore volume, which is capable of storing more metallic nanoparticles.
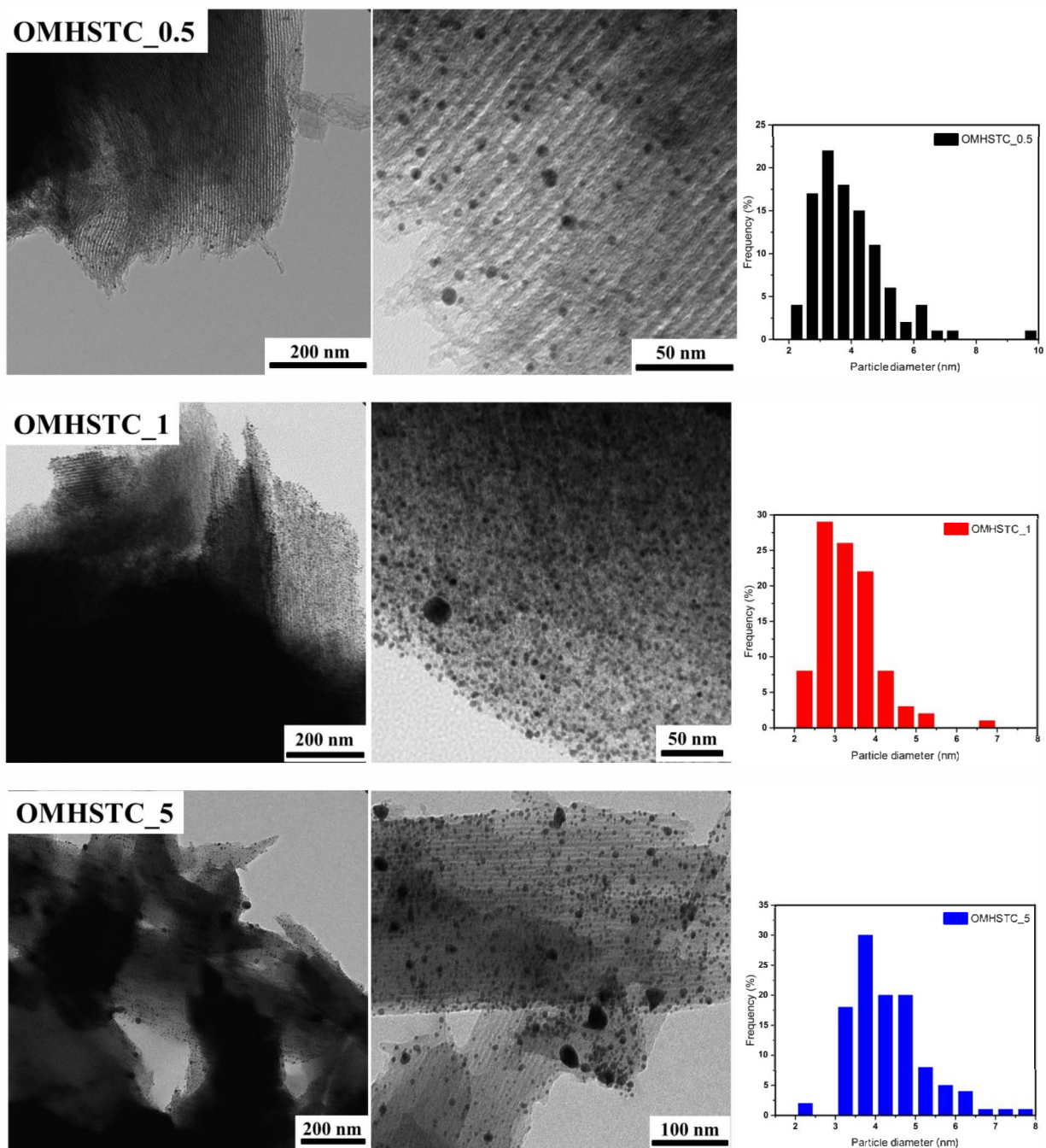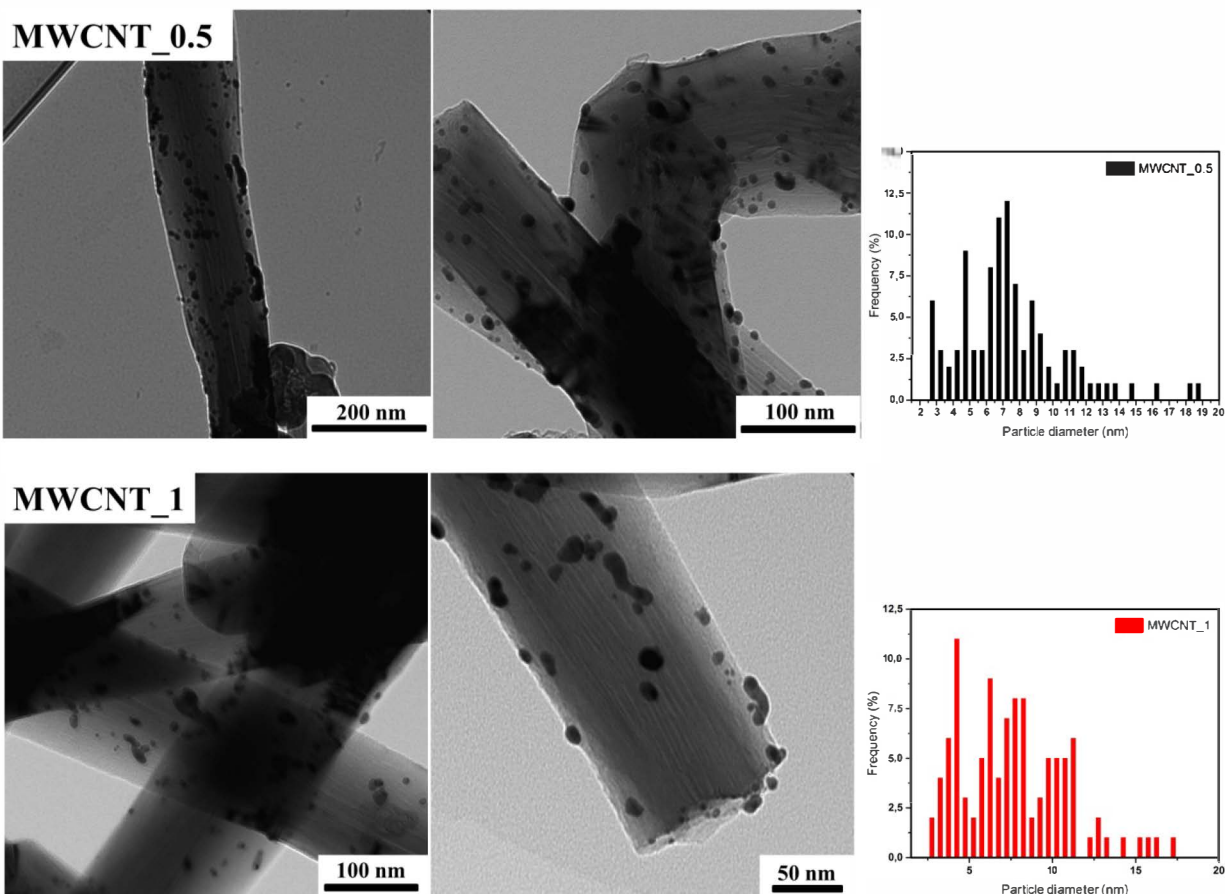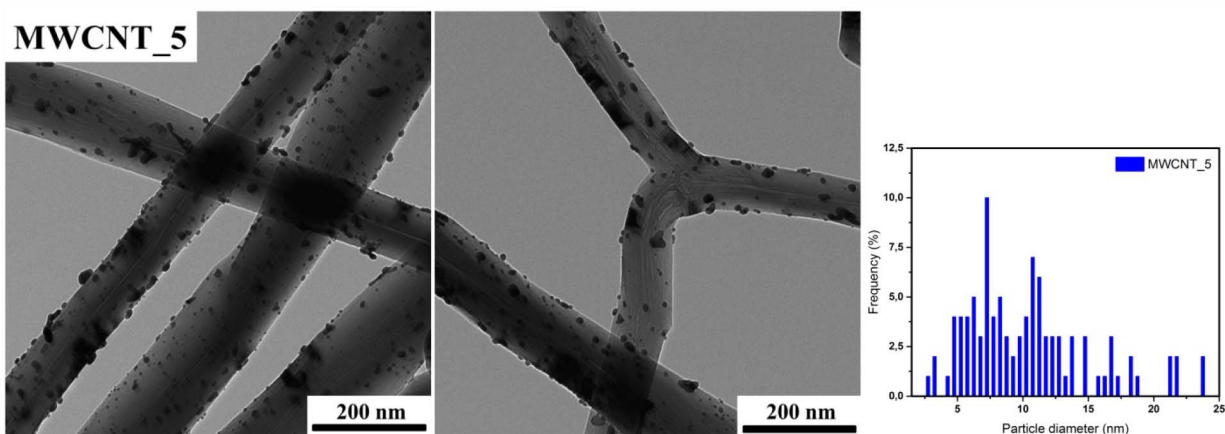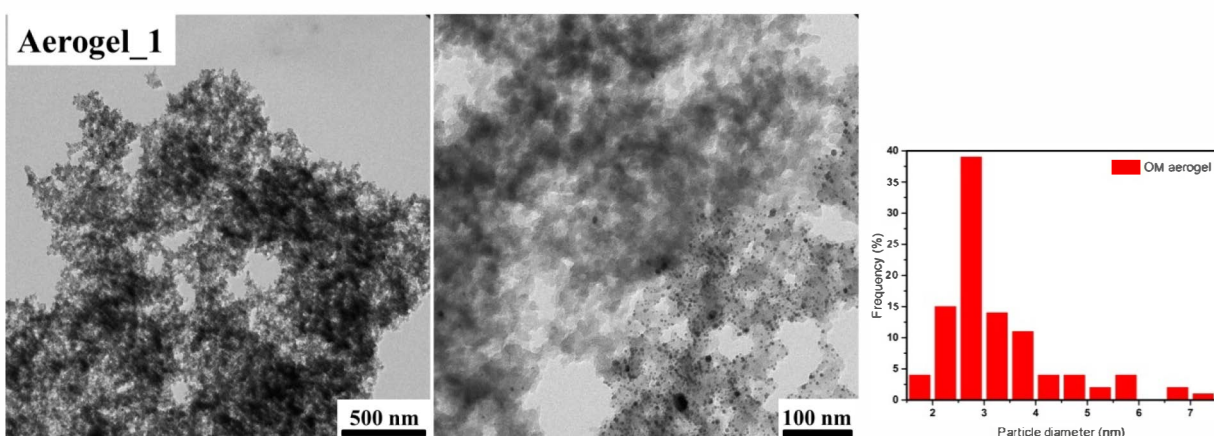

Figure 27. *TEM images of the catalysts OMHSTC_0.5 (top), OMHSTC_1 (middle), OMHSTC_5 (bottom) and the corresponding Au particle size distributions.*

MWCNT used for the catalyst synthesis have dimensions of 110-170 nm in diameter and 5-9 μm in length. As noted already from N_2 physisorption (**Figure 23**), this material exhibits only external porosity. From the obtained TEM data, this support seems to provide the best dispersion of gold nanoparticles, independent of Au loading, however their average size and PSD is not satisfactory for the catalytic purposes (**Figure 28**, **Table 6**). In all three MWCNT-supported AuNP catalysts, the nanoparticles are deposited on the external geometrical area of the CNT. The concave shape of the nanotubes implies that the surface available for gold deposition is not large enough. Moreover, the anchoring sites of other internally-porous carbons are stabilizing small metallic nanoparticles better, meaning that MWCNT external surface leads to agglomeration of deposited AuNP.

Figure 28. *TEM images of the catalysts MWCNT_0.5 (top), MWCNT_1 (middle), MWCNT_5 (bottom) and the corresponding Au particle size distributions.*

As already presumed from the nitrogen adsorption isotherms, TEM images for Aerogel present typical open-cell foam structure (**Figure 29**). Aerogel_1 gives rise to well-distanced small nanoparticles with an average size of 3.2 nm, which is the smallest size obtained in this work (**Table 6**). High external surface area of this highly disordered carbonaceous support is probably responsible for maintaining the gold nanoparticles of this size, with small statistical scattering (**Figure 29 (top)**). However, in the case of Aerogel_5, the loading of 1.05 wt. % is probably exceeding the "capacity" of the material's external surface for stabilizing small metallic particles, and the resulting catalyst is consisting of large AuNPs with broad size distribution (**Figure 29 (bottom)**).
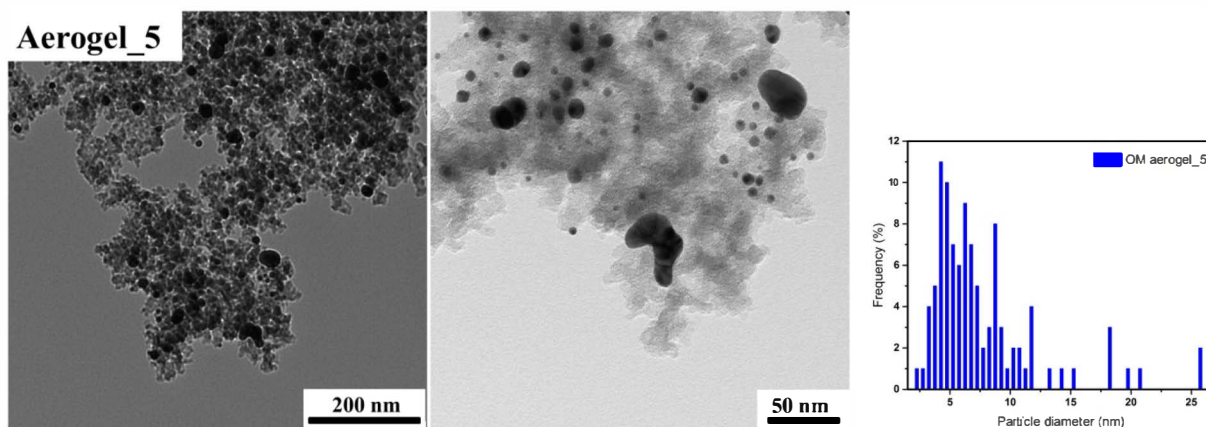
Figure 29. *TEM images of the catalysts Aerogel_1 (top), Aerogel_5 (bottom) and the corresponding Au particle size distributions.*

3.2.2 Catalytic Activity

The catalytic activity of the selected catalysts for the glucose oxidation reaction is tested for 50 mg of catalyst in 50 mL of glucose solution (0.1 mol/dm^3), on 45°C with stirring of 800 rpm. The solution is bubbled with oxygen (250 mL/min), and the pH value is kept at 9. The reaction is followed by titration with sodium hydroxide (1 mol/dm^3), therefore the volume of added NaOH vs. time is plotted in the graphs (**Figure 30**). The selectivity of the catalysts is estimated by analyzing the products of reaction by high performance liquid chromatography, which in the cases of full conversion resulted in total selectivity towards gluconic acid.

In **Figures 30** and **31**, the results of glucose oxidation reaction using carbon-supported catalysts are shown. What can be drawn as a general conclusion for all of the catalysts, is that a loading of 5 wt. % seems to be too high to obtain satisfactory catalytic activity. In the case of AC_5, the large diameter of the particles deposited on the support is not leaving enough of coordinately unsaturated positions on AuNP, therefore this catalyst is completely inactive. CMK-3_5 has very large particles, with broad distribution. The result is also an inactive catalyst. Reaction with OMHSTC_5 gave a very fast conversion, but since the loading is very high (2.99 wt. %), metal-time yield of this catalyst is low (**Figures 30** and **31**). MWCNT with all ranges of loadings (**Figure 30**) shows low catalytic activity, which is due to its low porosity, and a surface which is not appropriate for stabilization of small AuNPs. Aerogel_5's low activity can be attributed to large particles, with a lot of agglomerations. Among all catalysts except AC-supported series, 1

wt. % is the optimal loading, resulting in the highest MTY. Exceptionally good results that AC_0.5 exhibits are probably due to ICP measurement error, or the batch of the sample which has been examined by TEM. The average Au size of 9.5 nm (**Table 8**) theoretically cannot yield such a good activity (**Figure 30** and **31**). Moreover, the general trend of gold particle size according to the theoretical loading that all the other catalysts show is not followed in the case of AC, where the lowest loading gives the largest nanoparticles (**Table 8**). Due to generally high error in ICP measurements, the MTYs with theoretical gold loadings have been expressed in **Figure 31 (right)**. On the grounds of both theoretical and experimental MTY, it can be concluded that 1 wt.% is the most efficient gold loading examined. Moreover, OMHSTC is the only catalyst that can still deliver activity at high loading. The property of this catalyst support that a broad range of active catalytic phase can be loaded, while still remaining highly active, is really notable in terms of its versatility. To conclude, the combination of high surface of the material, together with a high volume of ordered mesopores, provides the most suitable support for AuNPs for the tested catalytic reaction.
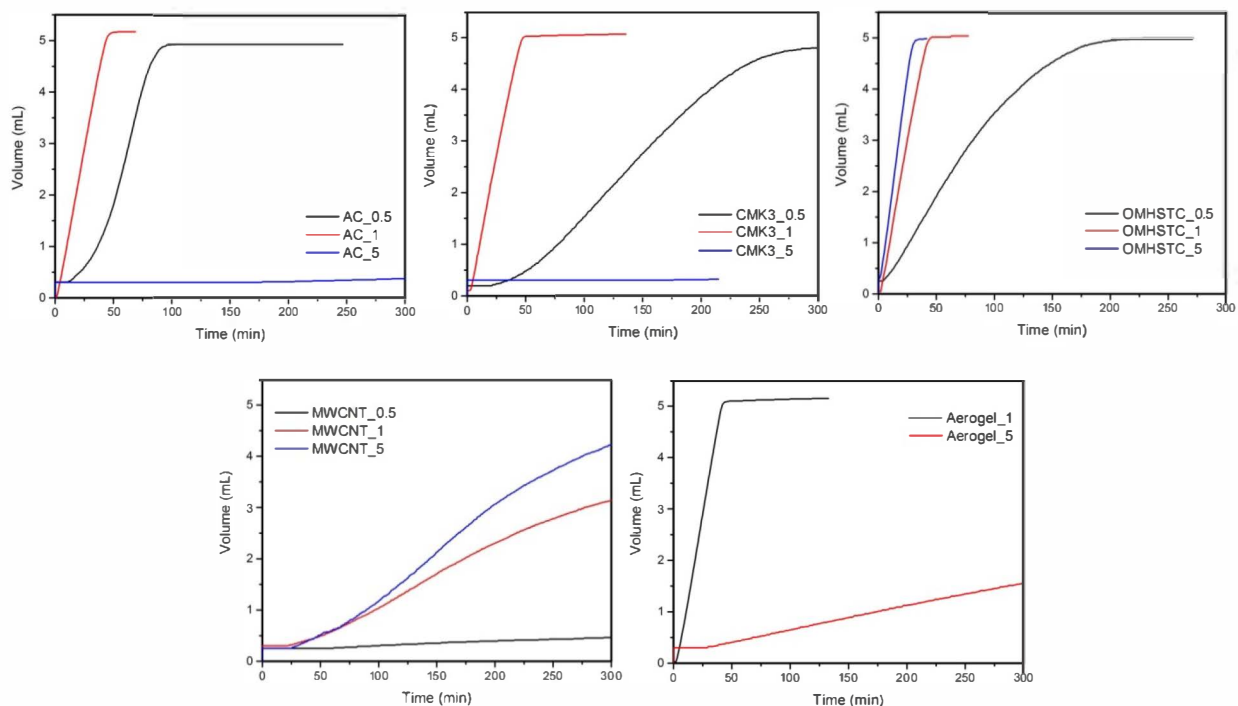
Figure 30. *Volume of added NaOH – time diagrams for the reaction of glucose oxidation using the synthesized catalysts.*
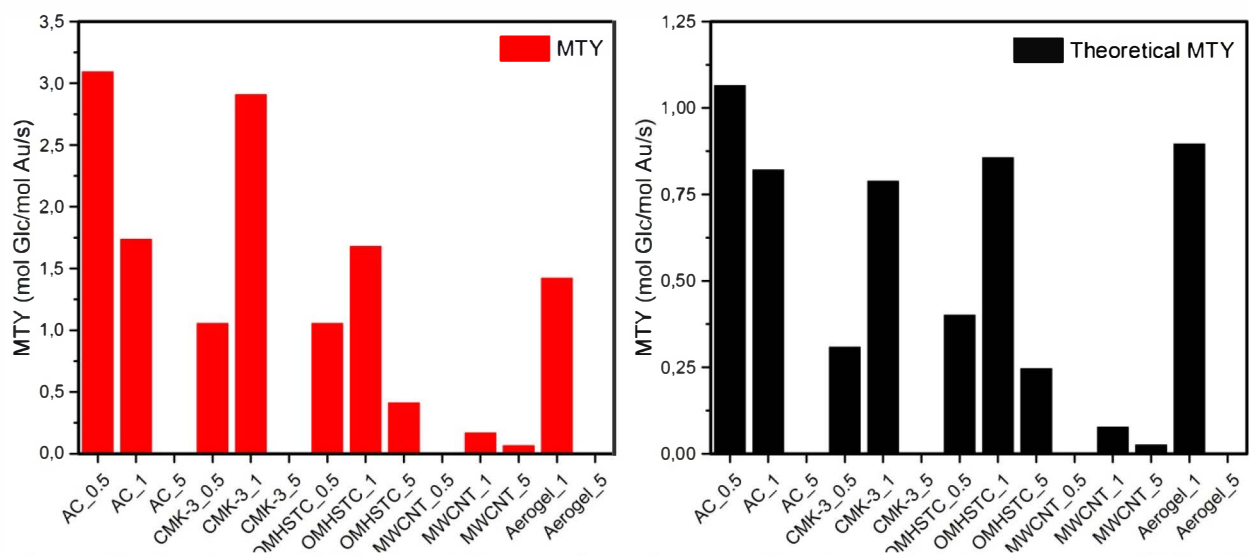
Figure 31. *Metal-time yield (left) and theoretical metal-time yield calculated with assumption of full gold deposition (right).*

Table 8. *ICP data summary, average Au particle sizes and gold-specific activity (expressed as metal-time yield, MTY) of the synthesized catalysts.*

Catalyst	Au (wt. %)$_{ICP}$	PSD (nm)	MTY (mol Glc/mol Au/s)
AC_0.5	0.17	9.5 ± 2.3	3.09
AC_1	0.47	4.4 ± 2.3	1.73
AC_5	0.90	7.6 ± 2.5	No conversion
CMK-3_0.5	0.15	N.A.	1.05
CMK-3_1	0.27	4.0 ± 2.3	2.90
CMK-3_5	0.52	7.7 ± 2.3	No conversion
OMHSTC_0.5	0.19	4.0 ± 1.2	1.05
OMHSTC_1	0.51	3.4 ± 1.0	1.68
OMHSTC_5	2.99	4.4 ± 0.9	0.41
MWCNT_0.5	0.24	7.6 ± 3.2	No conversion
MWCNT_1	0.46	8.0 ± 4.1	0.17
MWCNT_5	1.92	10.6 ± 4.9	0.06
Aerogel_1	0.63	3.2 ± 1.1	1.42
Aerogel_5	1.05	7.7 ± 4.6	No conversion

3.3 Glucose and Gluconic Acid Adsorption Experiments

In order to get insight to the adsorption abilities of the investigated catalyst supports, experiments on the adsorption of glucose and gluconic acid have been conducted. A series of solutions of glucose and gluconic acid with the same concentration and the same ratio of solution and the support as in catalytic tests have been prepared. After 5 h on 45°C and with stirring of 800 rpm, the sample of solution was taken in order to analyze the concentration.

A series of standard solutions of glucose and gluconic acid are prepared in order to record a calibration curve, though which the adsorption of these compounds on the tested supports could be concluded. **Figure 32b** shows that oxide supports, as well as hydrophobic carbon support (MWCNT) are adsorbing very low amounts of glucose. The fact that oxide supports do not adsorb glucose and thus their low conversion is not related to unwanted substrate immobilization strengthens the finding that carbon supports lead to higher activity of the gold nanoparticles that has been pointed out in the Chapter 3.1.2. Namely, low activity of these supports cannot be ascribed to the secondary effect of adsorption of the reactant, rather purely to poor support properties. On the other hand, OMHSTC and Aerogel are showing much larger uptake, which may be due to their high surfaces and abundant micropores with large adsorption potential for glucose. It is assumed that during the course of reaction, a small part of glucose from the solution is adsorbed on these materials, however when the concentration of glucose in solution decreases, the adsorbed amount diffuses back to the solution, where it is converted to gluconic acid. In the case of gluconic acid (**Figure 32d**), all of the supports were acting in a similar way, without notable adsorption of acid. It can thus be concluded that the product formed by glucose oxidation is immediately available for the titration and that the measured activity curves are also not influenced by unwanted product immobilization.
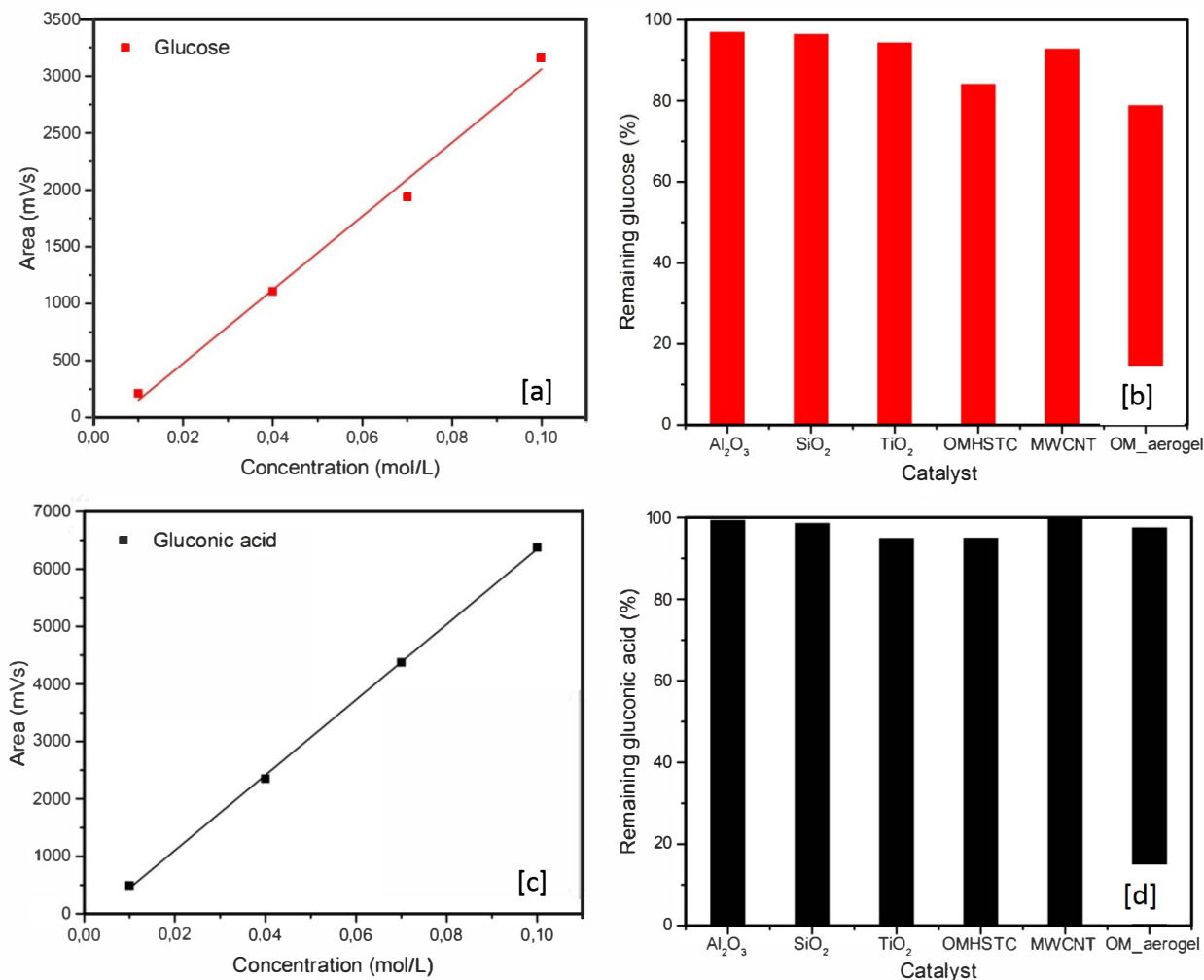
Figure 32. *Calibration curves [a], [c] and glucose and gluconic acid adsorption results on selected supports [b], [d].*

3.4 Mechanistic Studies on Glucose Oxidation Catalytic Reaction

Rate of catalytic reactions in general can be kinetically and diffusion controlled. If mass transport limitations strongly dominate the rate of reaction, the rate becomes equal to the mass transfer rate, i.e. the reaction is diffusion controlled. On the other hand, in kinetically controlled reactions, reaction rate is governed either by the amount of active ingredients or the total mass of the catalyst. In order to investigate the dominating mechanism of glucose oxidation reaction under the choosen conditions, a series of catalytic tests have been performed with different OMHSTC_1 catalyst loadings. **Figure 33** (left) shows volume of added NaOH vs. time diagram, and **Figure 33** (right) presents reciprocal of time needed for 80% of reactant to be converted as a function of catalyst mass. It can be observed that the speed of conversion shows near-linear

growth with increasing amount of employed catalyst. Hence, glucose oxidation reaction under tested conditions is not limited by mass transfer, and is therefore kinetically controlled. In consequence, it can be concluded that under the conditions of the reaction choosen in this work, the actual investigations of catalytic activity are not interferring with effects related to diffusion of reactants.
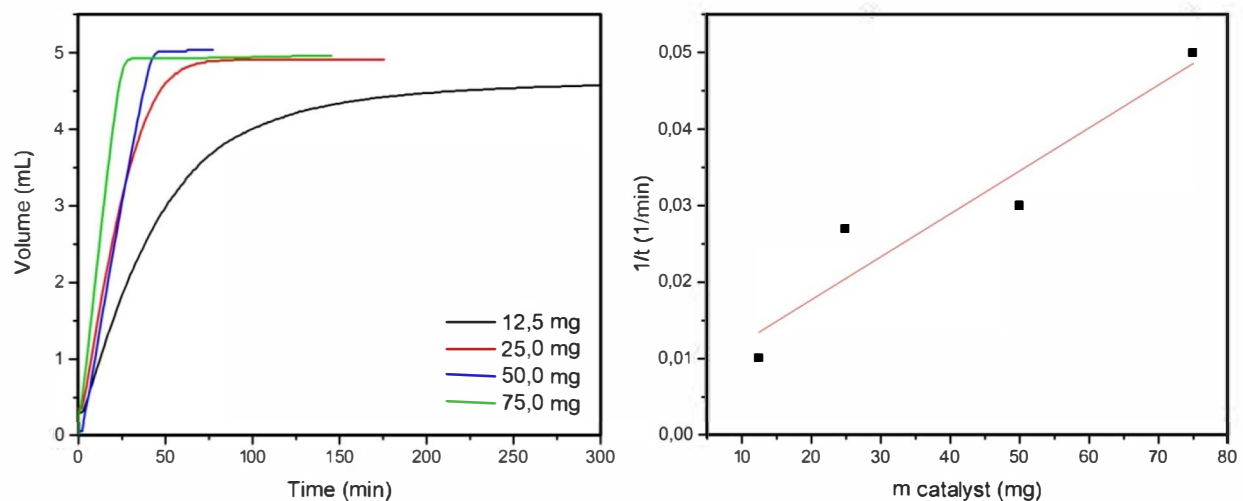
Figure 33. *Mechanistic studies on catalytic reaction of glucose oxidation.*

4. Conclusion and Outlook

Support effects on catalytic activity of heterogeneous gold nanoparticle catalysts for the selective oxidation of D-glucose to D-gluconic acid in aqueous solution with molecular oxygen have been investigated. Carbon materials have been proven to be much more advantageous as catalytic supports, in comparison to oxide supports (titania, alumina, silica). The reason for this is the surface chemistry of the oxide supports, namely their hydrophilicity and possible strong interaction with gold nanoparticles, which leads to low activity.

Moreover, the importance of mesoporous system in carbonaceous supports has been pointed out. High Au loadings are proven to be the least efficient for the series of carbon-supported catalysts due to larger particle sizes resulting from high loadings, whereas theoretical gold loading of 1 wt. % on carbon generally exhibits the highest catalytic activities. Series of catalysts that provide high metal time yield (up to 3 $mol_{glucose}/mol_{Au}/s$) for glucose oxidation reaction have been successfully synthesized. The most versatile catalyst support, offering broad range of possible Au loadings while preserving high catalytic activity is newly synthesized ordered mesoporous hard-salt templated carbon (OMHSTC) resulting from its large volume of ordered mesopores available for deposition of small gold nanoparticles.

Furthermore, catalytic glucose oxidation reaction in aqueous solution with molecular oxygen is confirmed to be kinetically controlled under the conditions utilized in this study and thus unwanted diffusion effects can be ruled out.

Finally, the findings on support-catalyst relationships from this work can be easily translated to different catalytic systems because there are numerous possibilities of using gold-on-carbon catalysts in gas and liquid phase reactions. Furthermore, carbon materials used in this thesis can be utilized as model supports for the synthesis of catalysts with other transition metals or bimetallic systems.

5. Experimental Section

5.1 List of Used Chemicals

Table 7. *List of used chemicals.*

Chemical	Formula	Purity	Supplier
D(+)-Glucose	$C_6H_{12}O_6$	≥99,5 %	Roth
Deuterium oxide	D_2O	"100%", 99.990 atom % D	Sigma Aldrich
D-Gluconic acid solution	$C_6H_{12}O_7$	49-53 wt. % in H_2O	Sigma Aldrich
Hydrogen tetrachloroaurate(III) trihydrate	$HAuCl_4 \cdot 3H_2O$	99.99%	Alfa Aesar
Sodium borohydride	$NaBH_4$	≥98.0%	Sigma Aldrich
Sodium citrate tribasic dihydrate	$HOC(COONa)(CH_2COONa)_2 \cdot 2H_2O$	≥99.0%	Sigma Aldrich
Sodiumhydroxide	$NaOH$	≥99.0%	Roth
Hydrochloric acid	HCl	37%	Roth
Zinc chloride	$ZnCl_2$	-	Sigma Aldrich
Pluronic® P-123	$EO_{20}PO_{70}EO_{20}$	-	Sigma Aldrich
Tetraethyl orthosilicate	$SiC_8H_{20}O_4$	98%	Sigma Aldrich
Sucrose	$C_{12}H_{22}O_{11}$	≥99.5%	Sigma Aldrich
Sulfuric acid, conc.	H_2SO_4	96%	Roth
Aeroxide® TiO_2 P 25	TiO_2	-	Evonik Industries
Aerosil® 380	SiO_2	-	Evonik Industries
Aeroxide® Alu 130	Al_2O_3	-	Evonik Industries
MWCNT	-	-	Sigma Aldrich
Activated carbon	-	-	Roth
Nitric acid	HNO_3	65%	Sigma Aldrich

5.2 List of Used Gases

Table 8. *List of used gases.*

Gas	Formula	Purity	Supplier
Oxygen 5.0	O_2	99,999%	Air Liquide
Hydrogen 3.0	H_2	99.9%	Air Liquide
Nitrogen 5.0	N_2	99.999%	Air Liquide
Helium 5.0	He	99.999%	Air Liquide
Argon 5.0	Ar	99.999%	Air Liquide

5.3 Materials Synthesis

5.3.1 Silica Template

Ordered Mesoporous SiO_2

The hexagonal ordered silica SBA-15 was synthesized by dissolving 48.78 g of the triblock copolymer Pluronic P123 ($EO_{20}PO_{70}EO_{20}$, Sigma Aldrich) in 885 g deionized water and 28.19 g concentrated aqueous hydrochloric acid solution over night at 35°C in a 1000 ml polypropylene bottle under intense stirring. Then, 104.86 g of tetraethyl orthosilicate (TEOS, 98%, Sigma Aldrich) were added to the solution and the mixture was stirred at 35°C for another 24 h. The white suspension was then transferred to a teflon-lined autoclave and hydrothermally treated at 115°C for 12 h followed by filtration and washing with ~2000 ml deionized water/ethanol (1:1 by volume). For complete removal of the structure-directing agent, the SBA-15 was calcinated at 550°C for 5 h in a muffle furnace (60 K/h heating rate). The SiO_2 yield is 95-98%.

5.3.2 Templated Carbon Materials

CMK-3

In a Petri dish, 4 g of the SBA-15 template (see section 4.3.1) were mixed with a 20 ml aqueous solution of 5 g sucrose to which was added 0.56 g 96% sulfuric acid. Polymerization of the carbohydrate was achieved by heating the mixture to 100°C for 6 h followed by subsequent

heating to 160°C for another 6 h. Complete infiltration of template pores was achieved by repeating the procedure described above with a 20 ml aqueous solution of 3.2 g of sucrose to which was added 0.36 g of 96% sulfuric acid, again followed by heating to 100°C and 160°C. Carbonization was carried out under flowing argon atmosphere in a horizontal tubular furnace. The material was heated to 900°C (heating rate: 150 K/h) and dwelled for 2 h. Silica removal was achieved by refluxing the carbonized composite material in sodium-hydroxide solution (400 ml, 5 mol/dm^3) overnight. After filtration and washing with large amounts of ethanol, the CMK-3 material was dried at 60 °C.

OMHSTC

4 g of SBA-15 was first impregnated with 16 mL of an aqueous solution of 5 g sucrose, 2.5 g ZnCl$_2$, and 0.56 g concentrated sulfuric acid in a petri dish. The mixture was then heated to 100 °C and held for 6 h followed by subsequent heating to 160 °C for another 6 h under air, in order to polymerize the carbohydrate molecules. Afterwards, the mixture was impregnated again with 12 mL of an aqueous solution of 3.2 g sucrose, 1.6 g ZnCl$_2$, and 0.36 g concentrated sulfuric acid, followed by the same heating regime. The polymerized carbohydrate was carbonized and the salt template was removed in a horizontal tubular furnace at 900 °C for 2 h under N$_2$ flow. The heating ramp was set to be 60 K/h from room temperature to 300 °C and 150 K/h from 300 to 900 °C. Silica removal was achieved by refluxing the carbonized composite material in sodium-hydroxide solution (400 ml, 5 mol/dm^3) overnight, followed by filtration, washing with large amounts of water and ethanol, and drying at 60 °C.

5.3.3 Colloidal Gold Dispersion

Gold nanoparticles were prepared using the preformed Au dispersion method. Hydrogen tetrachloroaurate(III) trihydrate (29.0 ml, 5.0783 mol/dm^3, 0.2 wt. %) is added to 500 ml of distilled water and is stirred in an Erlenmeyer flask. Sodium citrate tribasic dihydrate (11.6 ml, 34.0020 mol/dm^3, 1.0 wt. %) is quickly added to the solution to stabilize the AuNPs. 85 mg of sodium borohydride is added to ice-cold 1 wt. % sodium citrate solution. After 30 s, sodium borohydride in 1 wt. % of sodium citrate (5.8 ml, 44.9379 mol/dm^3) is added, in order to reduce AuNP to Au^0. The dispersion turned to red wine color indicating the formation of reduced

nanoparticles of gold. The final product is transferred to a glass bottle and kept in the fridge under absence of light.

5.3.4   Gold Deposition on Carbon Supports

In a typical procedure, 200 mg of the carbon/oxide support was added on top of previously prepared colloidal gold (see section 5.3.3) in a glass bottle. The bottle is sonicated for 2 h to secure equal adsorption of AuNP on the support. After 2 h, the red solution turns transparent, indicating full adsorption of the AuNPs. Later the catalyst is collected from the solution via centrifugation (4000 rpm for 20 min) and washed twice with distilled water. Finally, the catalyst is dried under vacuum (Thermo Scientific™ Vacutherm Vacuum Heating and Drying Oven) at $60^{o}C$ overnight. The final product was named X_Y, where X and Y represent the name of the carbon support and theoretical weight percentage of Au, respectively. The volumes of colloidal gold for preparation of 0.5 wt. %, 1 wt. % and 5 wt. % Au on 200 mg of carbon are 18.33 ml, 36.66 ml and 183.32 ml, respectively.

5.4 Catalytic Activity Test

The catalytic reaction of oxidation of glucose is operated via potentiometric titrator TitroLine® 6000/7000 device with the functionality of TITRONIC® piston burette (**Figure 34**). The titration system is equipped with three necked round bottom flask, to which the reflux funnel, pH meter electrode, oxygen inlet and sodium hydroxide standard solution inlet is connected. 50 mL of glucose (0.1 mol/dm^3) is added to the round bottom flask, which is placed in an oil bath and heated to $45^{o}C$, with stirring of 800 rpm. 250 mL/min oxygen is bubbled through the solution with a syringe. 50 mg of catalyst is added, and the reaction is started by keeping pH value of 9. The conversion of D-glucose to D-gluconic acid was investigated for 300 min for each catalyst. The catalytic activity was directly evaluated from the titration curve. It is expressed as metal time yield (MTY) in moles of converted glucose per mole of gold per second, and calculated from the average slope of the titration curve between 20 and 80 % glucose conversion.

Figure 34. *Catalytic reaction setup.*

5.5 Tests of Glucose and Gluconic Acid Adsorption on Catalyst

Series of standard solutions of glucose and gluconic acid are prepared (0.01, 0.04, 0.07 and 0.1 mol/dm^3), in order to record a calibration curve. In a typical procedure, 10 mg of catalyst was stirred in 10 mL of glucose/gluconic acid solution (0.1 mol/dm^3) in a closed bottle for 300 min at 45°C. Catalysts are separated from the solution after the test, via centrifugation and filtration. The solution is then analysed using high performance liquid chromatography (HPLC) with an Agilent 1200 spectrometer. The resulting signals were quantified by integrating the surface of the chromatographic peak for the corresponding compound. The results are interpreted using linear regression analysis.

5.6 Mechanistic Studies of Catalytic Reaction

Mechanistic studies are conducted in the same catalytic system under same conditions as described in section 4.4. Catalyst used for these tests was OMHSTC_1, with loadings of 12.5, 25, 50 and 75 mg in 50 mL glucose solution (0.1 mol/dm^3). Catalytic activity is calculated from the titration curve at the value of 80% glucose conversion.

5.7 Characterization Methods

5.7.1   Structural Characterization

Physisorption Measurements

Prior to all of the adsorption measurements, samples are outgassed under vacuum at 150°C for 20 h. Nitrogen physisorption experiments were carried out at −196°C on a Quadrasorb apparatus (Quantachrome Instruments, USA). Specific surface areas of the materials are calculated using the multipoint Brunauer–Emmett–Teller model in relative pressure range of 0.05 – 0.2. The total pore volume (V_t) is calculated by the Gurvich rule at a relative pressure of 0.99 for all carbons, except MWCNT and OM aerogel, for which relative pressure of 0.95 is used for calculation. In the case of oxide supports, V_t is calculated on a p/p_0 of 0.95. The pore size distributions are calculated using quenched solid density functional theory (QSDFT) method for nitrogen on carbon with slit/cylindrical/spherical pores at -196°C, adsorption branch kernel, integrated into the QuadraWin™ 5.11 analysis software (Quantachrome). Micropore volumes are calculated from the cumulative pore volumes at a diameter of 2 nm. Water vapor physisorption measurements are performed on a Quantachrome Autosorb IQ apparatus at 25°C.

Transmission Electron Microscopy

TEM studies were performed on a Zeiss EM 912Ω TEM microscope at an acceleration voltage of 120 kV. To prepare the TEM samples, catalysts were dispersed in ethanol, followed by dropping several droplets on a carbon-coated copper TEM grid and drying at room temperature. The particle size distribution was calculated manually using 100 Au particles per sample with software ImageJ 1.47v.

Small-angle X-ray scattering

SAXS was conducted with a Bruker AXS with CuKα1 radiation (0.154 nm).

Inductively coupled plasma-optical emission spectrometry

ICP-OES was conducted using a Horiba Ultra 2 instrument equipped with photomultiplier tube detection. The samples of catalysts with carbon support were burned off at 800 °C under air atmosphere, followed by dissolving the residual material in aqua regia. Oxide-supported catalysts were dispersed in aqua regia and filtered prior to analysis.

5.7.2   Analysis of the Product of Catalytic Reaction

High-Performance Liquid Chromatography

The products of the D-glucose oxidation reaction were analyzed using high performance liquid chromatography (HPLC) with an Agilent 1200 spectrometer. The products were separated over a Hypercarb column (150 x 4.6 mm) at a flow rate of 0.7 mL H_2O with 0.1 % formic acid as eluents (5 min isocratic, then a linear gradient to 20% acetonitrile (ACN) for 15 min, followed by a linear gradient to 100% ACN for 5 min.

6. Appendix

6.1 List of Figures

6.2 List of Tables

7. References

1.	Ertl, G.H.K., Ferdi Schüth, Jens Weitkamp, *HANDBOOK OF HETEROGENEOUS CATALYSIS*. **2008**, Weinheim, Germany: Wiley-VCH Verlag GmbH& Co. KGaA, Weinheim, Germany.
2.	Deutschmann, O., Kochloefl, K.H.K., Turek, T., *Heterogeneous Catalysis and Solid Catalysts*. **2009**.
3.	Thomas, J.M.T.a.W.J., *Principles and Practice of Heterogeneous Catalysis*. **2015**: Wiley-VCH Verlag GmbH & Co. KGaA, Boschstr. 12, 69469 Weinheim, Germany.
4.	Boudart, M., Davis, B.H., and Heinemann, H., *Introduction*, in *Handbook of Heterogeneous Catalysis*. 2008, Wiley-VCH Verlag GmbH. p. 1-48.
5.	Sabatier, P., Senderens, J. B., *C. R. Acad. Sci. Paris* **1902**, *134*, 514-516.
6.	Farrauto, C.H.B.a.R.J., *Fundamentals of Industrial Catalytic Processes,* 2nd edn. **2006**, Hoboken, NJ: Wiley Interscience.
7.	Herbschleb, C.T., *ReactorSTM : imaging catalysts under realistic conditions*, in *Faculty of Science*. 2011, Leiden University.
8.	Mars, P. and van Krevelen, D.W., *Chemical Engineering Science* **1954**, *3*, 41-59.
9.	Bond, G.C., Cunningham, R.H., and Slaa, J.C., *Topics in Catalysis* **1994**, *1*, 1, 19-24.
10.	Huang, D., Liao, F., Molesa, S., Redinger, D., and Subramanian, V., *Journal of The Electrochemical Society* **2003**, *150*, 7, G412-G417.
11.	Brown, S.D., Nativo, P., Smith, J.-A., Stirling, D., Edwards, P.R., Venugopal, B., Flint, D.J., Plumb, J.A., Graham, D., and Wheate, N.J., *Journal of the American Chemical Society* **2010**, *132*, 13, 4678-4684.
12.	Peng, G., Hakim, M., Broza, Y.Y., Billan, S., Abdah-Bortnyak, R., Kuten, A., Tisch, U., and Haick, H., *British Journal of Cancer* **2010**, *103*, 4, 542-551.
13.	Ali, M.E., Hashim, U., Mustafa, S., Che Man, Y.B., and Islam, K.N., *Journal of Nanomaterials* **2012**, *2012*, 7.
14.	Roduner, E., *Nanoscopic Materials: Size-Dependent Phenomena* **2006**. 298.
15.	Roduner, E., *Chemical Society Reviews* **2006**, *35*, 7, 583-592.
16.	Zhou, J., Ralston, J., Sedev, R., and Beattie, D.A., *Journal of Colloid and Interface Science* **2009**, *331*, 2, 251-262.
17.	Daniel, M.-C. and Astruc, D., *Chemical Reviews* **2004**, *104*, 1, 293-346.
18.	Turkevich, J., Stevenson, P.C., and Hillier, J., *Discussions of the Faraday Society* **1951**, *11*, 0, 55-75.
19.	Dimitratos, N., Lopez-Sanchez, J.A., and Hutchings, G.J., *Chemical Science* **2012**, *3*, 1, 20-44.
20.	Prati, L. and Rossi, M., *Journal of Catalysis* **1998**, *176*, 2, 552-560.
21.	Hu, Y., Wang, J., Zhao, R., Liu, Y., Liu, R., and Li, Y., *Chinese Journal of Chemical Engineering* **2009**, *17*, 3, 407-411.
22.	Zhang, T., Zhao, H., He, S., Liu, K., Liu, H., Yin, Y., and Gao, C., *ACS Nano* **2014**, *8*, 7, 7297-7304.
23.	Carrettin, S., McMorn, P., Johnston, P., Griffin, K., Kiely, C.J., and Hutchings, G.J., *Physical Chemistry Chemical Physics* **2003**, *5*, 6, 1329-1336.

24. Okatsu, H., Kinoshita, N., Akita, T., Ishida, T., and Haruta, M., *Applied Catalysis A: General* **2009**, *369*, 1, 8-14.
25. Haruta, M., *The Chemical Record* **2003**, *3*, 2, 75-87.
26. Hu, Y. and Dai, J., *Minerals Engineering* **2003**, *16*, 11, 1167-1172.
27. Haruta, M., Kobayashi, T., Sano, H., and Yamada, N., *Chemistry Letters* **1987**, *16*, 2, 405-408.
28. Haruta, M., *Catalysis Today* **1997**, *36*, 1, 153-166.
29. Vigneron, F. and Caps, V., *Comptes Rendus Chimie* **2016**, *19*, 1, 192-198.
30. Della Pina, C., Falletta, E., Prati, L., and Rossi, M., *Chemical Society Reviews* **2008**, *37*, 9, 2077-2095.
31. Haruta, M., *Gold Bulletin* **2004**, *37*, 1, 27-36.
32. Haruta, M. and Daté, M., *Applied Catalysis A: General* **2001**, *222*, 1, 427-437.
33. Y. Önal, S.S., and P. Claus, *Journal of Catalysis* **2004**, *223*, 122-133.
34. Philippe Serp, J.L.F., *Carbon Materials for Catalysis*. **2009**, Hoboken, New Jersey: John Wiley & Sons, Inc.
35. Auer, E., Freund, A., Pietsch, J., and Tacke, T., *Applied Catalysis A: General* **1998**, *173*, 2, 259-271.
36. Matthias Thommes, K.K., Alexander V. Neimark, James P. Olivier, Francisco Rodriguez-Reinoso, Jean Rouquerol and Kenneth S. W. Sing, *Pure Appl. Chem.* **2015**, *87*, 1051-1069.
37. Thune, E., Cabioc'h, T., Guérin, P., Denanot, M.F., and Jaouen, M., *Materials Letters* **2002**, *54*, 2, 222-228.
38. Zhang, W., Yao, M., Fan, X., Zhao, S., Chen, S., Gong, C., Yuan, Y., Liu, R., and Liu, B., *The Journal of Chemical Physics* **2015**, *142*, 3, 034702.
39. Kaneko, K., *Journal of Membrane Science* **1994**, *96*, 1, 59-89.
40. K. S. W. Sing, D.H.E., R. A. W. Haul, L. Moscou, R. A. Pierotti, J. Rouquerol, T. Siemieniewska, *Pure & Appl. Chem.* **1985**, *57*, 4, 603-619.
41. F. Rouquerol, J.R., K. Sing, *Adsorption by Powders and Porous Solids, Principles, Methodology and Applications*. **1999**, London: Academic Press.
42. Oschatz, M., *New Routes Towards Nanoporous Carbon Materials for Electrochemical Energy Storage and Gas Adsorption*, in *Fachrichtung Chemie und Lebensmittelchemie*. 2014, Technische Universität Dresden: Dresden. p. 208.
43. Zhang, Y., Li, B., Williams, K., Gao, W.-Y., and Ma, S., *Chemical Communications* **2013**, *49*, 87, 10269-10271.
44. Vissers, J.P.R., Lensing, T.J., De Beer, V.H.J., and Prins, R., *Applied Catalysis* **1987**, *30*, 1, 21-31.
45. Martí'n-Gullón, A., Prado-Burguete, C., and Rodríguez-Reinoso, F., *Carbon* **1993**, *31*, 7, 1099-1105.
46. Donnet, J.-B., *Carbon Black: Science and Technology, Second Edition*. **1993**.
47. Marsh, H. and Rodríguez-Reinoso, F., *CHAPTER 1 - Introduction to the Scope of the Text*, in *Activated Carbon*. 2006, Elsevier Science Ltd: Oxford. p. 1-12.
48. Rodríguez-Reinoso, F., *Production and Applications of Activated Carbons*, in *Handbook of Porous Solids*. 2008, Wiley-VCH Verlag GmbH. p. 1766-1827.
49. McEnaney, B., *Properties of Activated Carbons*, in *Handbook of Porous Solids*. 2008, Wiley-VCH Verlag GmbH. p. 1828-1863.
50. Jun, S., Joo, S.H., Ryoo, R., Kruk, M., Jaroniec, M., Liu, Z., Ohsuna, T., and Terasaki, O., *Journal of the American Chemical Society* **2000**, *122*, 43, 10712-10713.

51. Lee, J., Sohn, K., and Hyeon, T., *Journal of the American Chemical Society* **2001**, *123*, 21, 5146-5147.
52. Ryoo, R., Joo, S.H., and Jun, S., *The Journal of Physical Chemistry B* **1999**, *103*, 37, 7743-7746.
53. Yan, R., Heil, T., Presser, V., Walczak, R., Antonietti, M., and Oschatz, M., *Advanced Sustainable Systems* **2017**.
54. Fechler, N., Fellinger, T.P., and Antonietti, M., *Adv Mater* **2013**, *25*, 1, 75-9.
55. Cañete-Rodríguez, A.M., Santos-Dueñas, I.M., Jiménez-Hornero, J.E., Ehrenreich, A., Liebl, W., and García-García, I., *Process Biochemistry* **2016**, *51*, 12, 1891-1903.
56. Serena Biella, L.P., Michele Rossi, *Journal of Catalysis* **2002**, *206*, 242–247.
57. Dimitratos, N., Lopez-Sanchez, J.A., and Hutchings, G.J., *Topics in Catalysis* **2009**, *52*, 3, 258-268.
58. Besson, M. and Gallezot, P., *Catalysis Today* **2000**, *57*, 1-2, 127-141.
59. Comotti, M., Della Pina, C., Matarrese, R., and Rossi, M., *Angew Chem Int Ed Engl* **2004**, *43*, 43, 5812-5.
60. Baatz, C. and Prüße, U., *Journal of Catalysis* **2007**, *249*, 1, 34-40.
61. Baatz, C., Decker, N., and Prüße, U., *Journal of Catalysis* **2008**, *258*, 1, 165-169.
62. Porta, F., Prati, L., Rossi, M., Coluccia, S., and Martra, G., *Catalysis Today* **2000**, *61*, 1, 165-172.
63. Beltrame, P., Comotti, M., Della Pina, C., and Rossi, M., *Applied Catalysis A: General* **2006**, *297*, 1, 1-7.
64. Claudia L. Bianchi, S.B., Antonella Gervasini, Laura Prati, Michele Rossi, *Catalysis Letters* **2003**, *85*, 91-96.
65. Mirescu, A., Berndt, H., Martin, A., and Prüße, U., *Applied Catalysis A: General* **2007**, *317*, 2, 204-209.
66. Mirescu, A. and Prüße, U., *Catalysis Communications* **2006**, *7*, 1, 11-17.
67. Zhao, D., Feng, J., Huo, Q., Melosh, N., Fredrickson, G.H., Chmelka, B.F., and Stucky, G.D., *Science* **1998**, *279*, 5350, 548-552.